Glutathione-Enhanced Magnetic Hyperthermia

Exploring the Effect of Glutathione on the Heating Efficiency of Magnetic Nanoparticles for Cancer Treatment

Bachelor Research Project

Rebecca Jekel

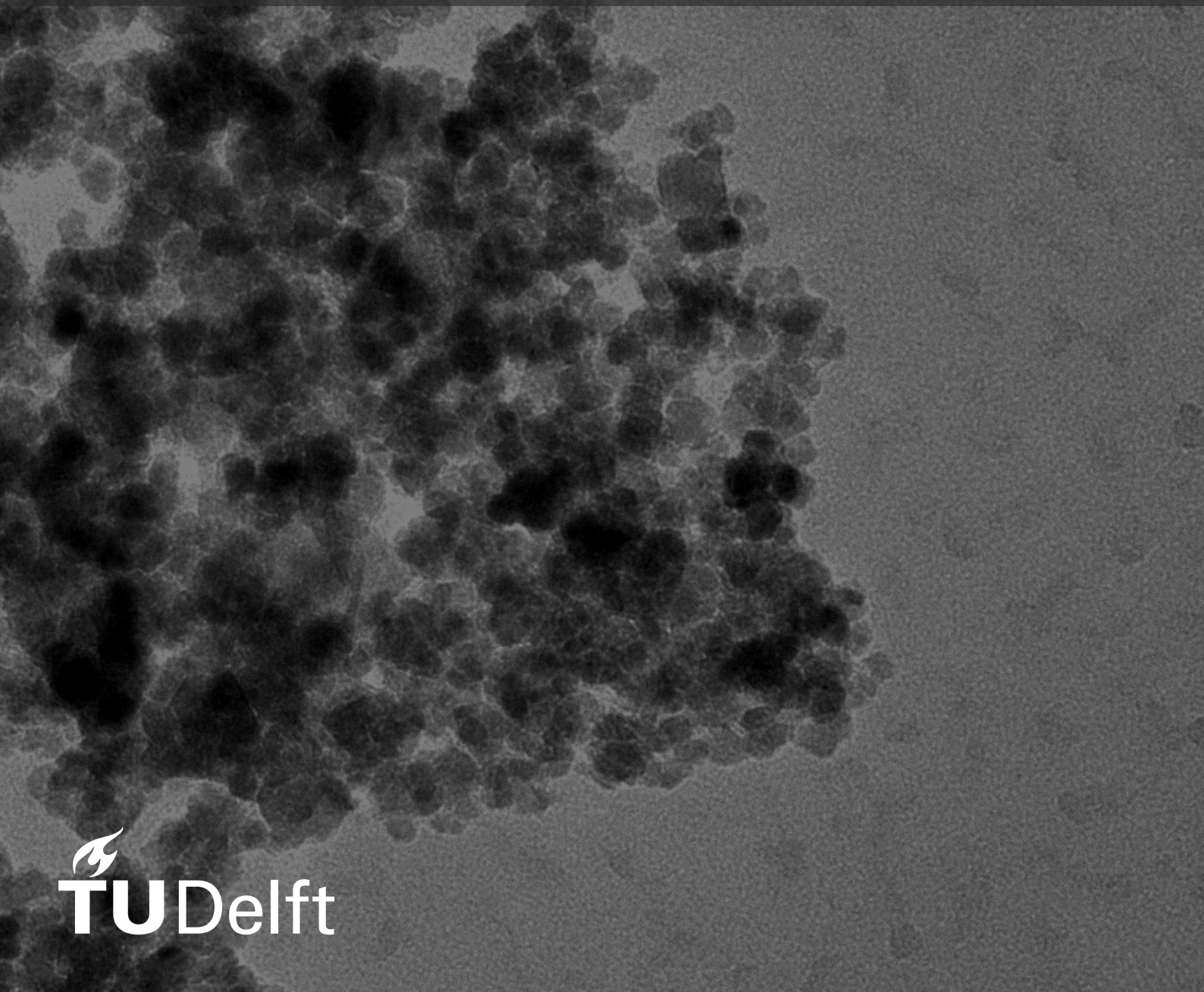

TU Delft

Glutathione-Enhanced Magnetic Hyperthermia

Exploring the Effect of Glutathione on the Heating Efficiency of Magnetic Nanoparticles for Cancer Treatment

by

Rebecca Jekel

Student Name	Student Number
Rebecca Jekel	5241162

Responsible Thesis Supervisor:	Kristina Djanashvili
Second Examiner:	Antonia Denkova
PhD candidate:	Qi Jia
Project Duration:	April, 2024 - July, 2024
Departments:	Radiation Science and Technology Biotechnology

TU Delft

Preface

This thesis marks the end of my Bachelor in Life Science and Technology at Delft University of Technology and Leiden University. It was completed at the Applied Radiation and Isotopes (ARI) group in the department Radiation Science and Technology.

My thesis would not have been possible without the support of my supervisors. First of all, thank you Qi Jia for all your time and advice. Secondly, thank you Kristina Djanshvili for your supervision, advice and fun conversations. Thank you, Antonia Denkova for providing valuable second opinions. Eline van den Heuvel, thank you for your training in DLS and your and Melanie Zorrón Pless' support in analysing the results. I would like to thank Baukje Terpstra as well for the ICP measurements, Qi Jia and Gauri for the FTIR measurements and Qi Jia for the TEM measurements. And a huge thank you to my office mates Sarah and Ilse for making my lunch and coffee breaks more fun!

Thank you all. I hope that our paths will cross in the future again.

Rebecca Jekel
Delft, July 2024

Abstract

Female breast cancer is the second most common cancer worldwide. A promising novel technique to treat early-stage breast cancer is the use of thermo-brachy therapy. This thesis analysed the effect of the cancer biomarker glutathione (GSH) on the magnetic hyperthermal effects of iron oxide nanoparticles. The synthesised nanoparticles with a diameter of 10±4 nm have been coated with cysteine and treated with hydrogen peroxide leading to their aggregation upon cross-linking. As the GSH concentration is higher around cancerous cells (10 μM instead of 3 μM), these nanoparticles would be more monodispersed as GSH could break the disulfide bonds between the cysteines. Since aggregated nanoparticles exhibit lower heating efficiencies, it was assumed that this method would allow for (partially) selective heating of the tumour. The addition of 10 μM GSH resulted in an 11% higher heating efficiency compared to 3 μM GSH when analysing the coated nanoparticles in an alternating magnetic field. However, a GSH concentration of 10 mM (intracellular GSH concentration in cancerous cells) gave a decrease in heating efficiency.

Another methodology was proposed as well. Uncoated nanoparticles were encapsulated in a ZIF-8 framework. This framework is less stable in environments with a lower pH value and higher GSH concentration, which is the case in the tumour microenvironment. This methodology gave a 27% higher heating efficiency in a tumour-related GSH concentration and pH value.

The differences with both the cysteine and ZIF-8-based methods are yet too small to limit thermal damage to healthy tissue. Modelling the diffusion and its influence on the temperature change, gave very local heating near the injection site due to slow diffusion. Therefore, while this thesis provided insights into the heating efficiencies in tumour-related conditions with both methodologies, addressing the current limitations can lead to significant advancements.

Contents

Nomenclature

Abbreviations

Abbreviation	Definition
DLS	Dynamic Light Scattering
FTIR	Fourier-transform Infrared Spectroscopy
GSH	Glutathione
GSSH	Glutathione dimer
ICP-MS	Inductively Coupled Plasma Mass Spectroscopy
ILP	Intrinsic Loss Power
MNP	Magnetic nanoparticles
MOF	Metal-organic framework
MRI	Magnetic Resonance Imaging
PGLA	Poly(d, l-lactide-co-glycolic acid)
PVA	Polyvinyl alcohol
ROS	Reactive oxygen species
SAR	Specific Absorbance Rate
SLP	Specific Loss Power
SPIONs	Superparamagnetic iron oxide nanoparticles
TEM	Transmission Electron Microscopy
TME	Tumour microenvironment
ZIF-8	Zeolitic imidazolate framework-8

Symbols

Symbol	Definition	Unit
A	Area under hysteresis cycle	[kg m^2/s^2]
C_p	Specific heat capacity	[J/kg K]
D	Diffusion coefficient	[m^2/s]
f	Frequency	[Hz]
H	Magnetic field intensity	[A/m]
k_B	Boltzmann constant	[m^2 kg/s^2 K]
m	Mass	[g]
M_s	Saturation magnetisation	[emu/cc]
P	Dissipation power	[W]
Q	Heat energy	[J]
R_H	Hydrodynamic radius	[m]
SAR	Specific Absorbance Rate	[W/g]
SLP	Specific Loss Power	[W/g]
T	Temperature	[K]
t	Time	[s]
η	Viscosity	[Pa s]
τ	Decay time	[µs]

1 Introduction

This Bachelor Thesis explores the magnetic hyperthermal properties of iron oxide nanoparticles for a novel approach for targeted, localised heating thermo-brachy treatment of cancer.

1.1. Cancer and the tumour microenvironment

The World Health Organization registered 9.7 million deaths caused by cancer in 2022, making it one of the leading causes of death worldwide [1]. Among all types of cancer, female breast cancer was found as the second most common, with 2.3 million new cases (11.6%). Due to the global population ageing and growth, combined with an increase in tobacco, alcohol, obesity and air pollution, this report predicted over 35 million new cases of cancer by 2050 (increase of 77%).

Cancer is characterised by uncontrollable cell division of the patient's own cells. Normally, many control steps are present during cell replication and division to avoid unwanted DNA mutations, for instance. Cancerous cells display fewer control steps, lack growth- and apoptosis-mediated signals and can invade other areas of the body and therefore spread. The tumour microenvironment (TME) is the ecosystem around a tumour composed of cancerous cells. Next to the cancerous cells, many immune and stromal cells, blood vessels and an extracellular matrix are present [2]. The TME is characterised by nutrient deprivation, cytokines, growth factors, chemokines, matrix remodelling enzymes and metabolites. Besides that, the TME has a lower extracellular pH (6.5) compared to normal cells (7.4) and a higher intracellular pH (7.4) compared to normal cells (7.2) due to an elevated need demand for glycolysis in cancer cells (acidosis) [3] [4]. Cancerous cells also display hypoxia, a limited amount of oxygen due to the rapid cell proliferation.

The acidosis and hypoxia are not only a result of the tumour's metabolism, but also play an important role in affecting the redox status, and therefore also induce higher concentrations of glutathione (GSH) in the TME [5]. GSH is a negatively charged tripeptide consisting of cysteine, glutamate and glycine. Cancerous cells have a higher level of reactive oxygen species (ROS) due to their hypoxia [6]. Low to moderate levels of ROS act as second messengers in cell signalling and are therefore essential to normal and cancerous cells to support growth and proliferation [7]. However, at high levels, ROS can harm the cells and therefore cause cell death [8]. GSH acts as a regulator of the cellular redox state and can remove and detoxify the enlarged amounts of carcinogenic ROS produced due to extraordinary metabolic rates in normal, non-cancerous cells [6]. However, in cancerous cells, GSH does not only protect the cell against this oxidative stress but is also synthesised after induction with tumour promotors such as NRF2 [9]. Non-cancerous cells have an intracellular GSH concentration of 1-10 mM [10] and an extracellular concentration of 2-4 µM [11]. Cancerous cells have an intracellular GSH concentration of 2-10 mM [12] and an extracellular concentration of 2-20 µM [13].

1.2. Common cancer treatments and their limitations

The primary therapies to treat cancer are surgery, chemotherapy and radiotherapy [14]. Main drawbacks of surgery, are that it can only be performed in case the tumour is well-localised and well-

accessible and that it could also induce infections or damage nearby healthy tissue. Chemotherapy targets the entire body, which is beneficial in cases of metastatic cancer, where the cancer has spread to other parts of the body. During chemotherapy, drugs are used to treat fast-growing cells. However, not only cancer cells but also hair follicles, cells in the bone marrow and cells in the digestive tract also display rapid growth. Therefore, side effects include hair loss, fatigue and nausea. Radiation therapy uses high-energy particles or waves to target cancer cells by damaging the DNA. External radiation therapy uses a beam that emits photons, protons or electrons towards the tumour. Internal radiation can be achieved through intravenous injections of radionuclides. Currently, this is used in palliative care [15] and pre-clinical research only [16]. Another way to achieve internal radiation therapy is with the use of brachytherapy, as is further described in Section 1.3.

1.3. Brachytherapy and hyperthermia

More novel therapy methods to treat cancer are brachytherapy and hyperthermia. Brachytherapy is a local radiation technique in which small amounts of encapsulated radioactive material are injected into or near the tumour. This allows for local eradication of cancerous tissue. The main advantage of this method compared to the traditional radiation method, is that the radiation dose is high near the tumour, but lower in the surrounding healthy tissue and therefore limits damage to healthy tissue. An important drawback of this method is that the tumour area needs to be small, accessible (not deep-seated) and well-localised [17]. Therefore, brachytherapy can only be used in the early stages of cancer, where the tumour is relatively small and has not yet spread to other areas in the body. Another major drawback is that cancerous cells can be radioresistant, which is also caused by hypoxia [18].

One way to decrease the radioresistance of cancerous cells is with the use of thermal ablation or hyperthermia. With thermal ablation, these cells are heated to temperatures around 48-50°C, resulting in cell death within minutes. Hyperthermia heats these cells to temperatures of 44-46°C, which can eradicate the tumour as well. However, cancerous cells are more susceptible to external heat than non-cancerous cells. In tumours, the blood vessel network is less efficiently organised and therefore the heat cannot be dissipated as effectively [19]. Secondly, acidosis also contributes to the heat sensitivity of cancerous cells [20]. This causes hyperthermia to damage cancerous cells quite effectively with a limited impact on non-cancerous cells. Hyperthermia can also be combined with brachytherapy in a technique called thermo-brachytherapy. In thermo-brachytherapy, the cancerous cells are not only heated but are exposed to hyperthermic radiosensitization as well, meaning the tumour is more susceptible to radiation-induced damage and therefore a more effective cancer treatment [21] [22].

1.4. Magnetic nanoparticles

Thermo-brachytherapy can be achieved using magnetic nanoparticles (MNP). MNP have a diameter between 1 and 100 nm and can be manipulated by alternating magnetic fields and are therefore magnetic [23]. MNP can consist of two components, a magnetic shell and a chemical compound within. This can for instance be achieved with MNP with an iron oxide (Fe_3O_4) shell containing a radioactive material within. In previous research, palladium-103 has been used as a radioactive core [24]. Iron oxide nanoparticles are considered to have good biocompatibility (non-cytotoxic and non-genotoxic) [25]. Iron oxide also has a relatively low heating capacity, meaning that iron oxide's temperature can be raised with a relatively low amount of (electromagnetic) energy, which is beneficial for the use of these MNP in hyperthermia [26]. Since a radioactive material is also present in the MNP, these particles can be used for brachytherapy as well. Therefore, the dual composition of the MNP allows for dual cancer treatment with thermo-brachytherapy. However, this thesis uses nanoparticles composed of only iron oxide in order to analyse its magnetic hyperthermal effects.

In this thesis, MNP will be synthesised using co-precipitation. Iron(II) and iron(III) chloride are slowly combined with ammonium hydroxide, after which the following reaction will take place.

$$FeCl_2 + 2\ FeCl_3 + 8\ NH_3 + 4\ H_2O \rightarrow Fe_3O_4 + 8\ NH_4^+ + 8\ Cl^-$$

The precipitation of Fe^{3+} occurs at a low pH at the beginning of the synthesis, while Fe^{2+} precipitation tends to happen at a high pH. Because of this, hydroxide is added slowly to ensure both ions will precipitate, therefore the name co-precipitation. The ammonium ions also prevent aggregation of the synthesised particles.

The aggregation state of MNP can be influenced by altering the surface chemistry of the MNP. After synthesis, the MNP have hydroxide groups covalently bound to the surface. These groups stabilise the surface of the MNP [27]. In this thesis, the hydroxide groups are replaced by covalently bound cysteine. If these cysteines are not linked with each other, the MNP are monodispersed. Cysteines can form disulphide bonds in the presence of the oxidising agent hydrogen peroxide (H_2O_2), thus resulting in interlinked or aggregated MNP. Aggregation of MNP alters the effective size of the MNP and thus the properties of the MNP (further explained in Section 1.6.1) [28]. Overexpression of GSH can reduce the disulphide bonds by thiol-disulfide exchange and therefore redisperse the MNP once again [29]. The GSH itself will present in its oxidised glutathione dimer form (GSSH) after reducing the disulfide bonds.

This mechanism is presented in Figure 1.1.

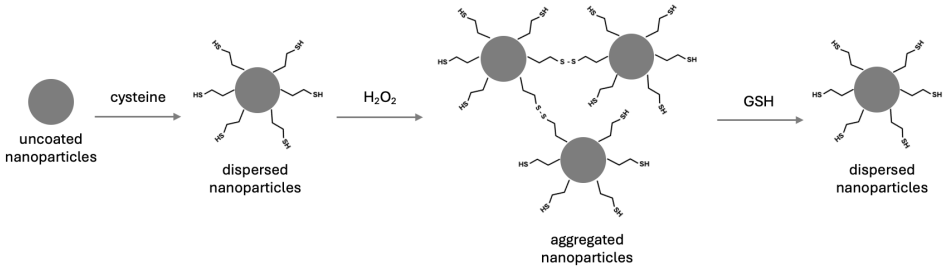

Figure 1.1: Aggregation and dispersion mechanism of the cysteine coated nanoparticles upon addition of hydrogen peroxide and GSH.

1.5. Surface characterisation and size analysis

To analyse the size distribution and surface chemistry of the nanoparticles, the following techniques were used.

1.5.1. Dynamic Light Scattering (DLS)

First, the hydrodynamic size of the particles was analysed using Dynamic Light Scattering (DLS). DLS is a technique that can be used to determine the hydrodynamic radius of small (between 1 and 2500 nm) particles in a suspension.

DLS analyses the Brownian motion, the random movement of particles in a solution, which strongly depends on the size of the particles. A laser passes through the solution and is therefore scattered by the particles in the solution. At every time point, the amount of light scattered at a certain angle is measured. Large particles have a slower Brownian motion, therefore this signal fluctuates less over time compared to smaller particles. This in ity signal over time is then converted to an intensity correlation function, see Figure 1.2.

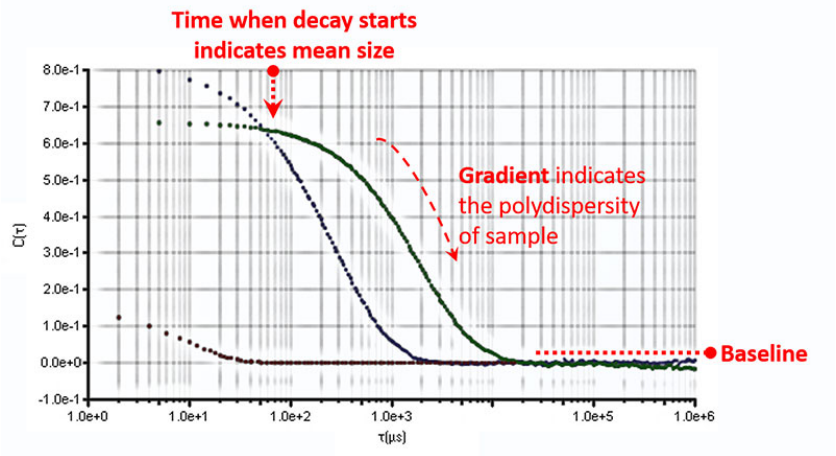

Figure 1.2: Example of an intensity correlation function with its parameters explained [30].

Figure 1.2 shows the intensity correlation function C(τ) against τ, the decay time. From this graph, the diffusion coefficient (*D*) is determined, which is directly correlated to the hydrodynamic radius (R_H) as presented in Equation 1.1.

$$R_H = \frac{k_B T}{6\pi\eta D} \tag{1.1}$$

Here, k_B represents the Boltzmann constant, *T* the temperature in Kelvin and η the viscosity. The hydrodynamic radius is usually larger than the physical radius of a particle since it also takes interactions at the particle's surface into account (surfactants).

1.5.2. Transmission Electron Microscopy (TEM)

Transmission Electron Microscopy (TEM) is a technique in which an electron gun transmits electrons through an electromagnetic lens towards the sample. The sample interacts with the electrons, after which these pass through two more electromagnetic lenses and form an image on a fluorescent screen or a detector. This technique allows for a resolution around 0.1 nm. In this thesis, TEM is mainly used to analyse the physical diameter of the particles.

1.5.3. Fourier-transform infrared spectroscopy (FTIR)

Fourier-transform infrared spectroscopy (FTIR) does not only analyse the composition of elements in a sample, but also the interaction between these elements. An infrared light is pointed towards the sample, which is partially absorbed by the sample. FTIR analyses the intensity of the light before and after absorption. Therefore, FTIR can be used to analyse the interactions of the thiol groups in the cysteine coating.

1.6. Heating efficiency of the magnetic nanoparticles

Magnetic hyperthermia is the conversion of electromagnetic energy into heat mediated by the MNP, which is caused by the coupling of the magnetic moments of the MNP's atoms with the applied time-varying external magnetic field. The specific loss power (SLP), which is equal to the specific absorbance rate (SAR), describes the heat rate at which a magnetic material absorbs electromagnetic energy and converts it to heat and therefore represents the heating efficiency. In the case of MNP, a high SLP value would be ideal, since a high SLP value would result in a lower dose of MNP needed for hyperthermal treatment.

Equation 1.2 displays that SLP and therefore SAR are related to the dissipation power (*P*) and the density of the MNPs (*r*). The dissipation power is equal to the area of the hysteresis cycle recorded under the applied alternating magnetic field and (*A*) and the alternating frequency of this field (*f*)

$$\text{SLP} = \text{SAR} = \frac{P}{r} = \frac{Af}{r} \tag{1.2}$$

However, it is important to note that this SLP is an equipment-specific measure since it highly depends on the amplitude and frequency of the alternating magnetic field. Therefore, the intrinsic loss power (ILP) is also introduced. Equation 1.3 shows that the ILP is defined as the ratio of SAR to $H^2 f$.

$$\text{ILP} = \frac{\text{SAR}}{H^2 f} \tag{1.3}$$

Equation 1.3 is valid for frequencies up to several MHz and for amplitudes of the magnetic field below the saturation field of the MNP [31].

In order to calculate the SLP, the amount of iron oxide in the suspension has to be known. After the heating experiments, Inductively Coupled Plasma Mass Spectroscopy (ICP-MS) was performed, which uses an ionised plasma by heating helium and analyses the resulting ions with mass spectroscopy.

1.6.1. Requirements on the size of the nanoparticles

In this thesis, the nanoparticles were aimed to have a diameter of 13-15 nm. Particles that would have a lower diameter than 13 nm would also have a smaller magnetic core diameter. Larger individual particles result in higher SLP values up to a certain diameter [32]. This is because the SLP value is linearly correlated to *A* (Equation 1.2) and *A* in its turn to the saturation magnetization (M_S). M_S is then linearly correlated to the magnetic core diameter. Previous literature found that an increase in diameter from 8 to 13 nm (increase of 63%) can increase the SLP value from 10 to 58 W/g (increase of 480%) when analysing iron oxide spherical nanoparticles from a co-precipitation synthesis [33].

However, particles with a too-large diameter are also not desired for magnetic hyperthermal therapy for the following four reasons.

Firstly, the nanoparticles can exhibit superparamagnetic behaviour and therefore are superparamagnetic iron oxide nanoparticles (SPIONs) up to a diameter of a few tens of nanometers. SPIONs can respond rapidly to an alternating magnetic field but lose its magnetisation after this field is removed [34]. This is highly necessary when using nanoparticles for thermo-branchy therapy with regards to patient safety. Larger particles can have multiple magnetic domains and thereby become ferromagnetic, meaning that they typically exhibit a hysteresis loop instead of showing a sigmoid curve, as can be seen in Figure 1.3.

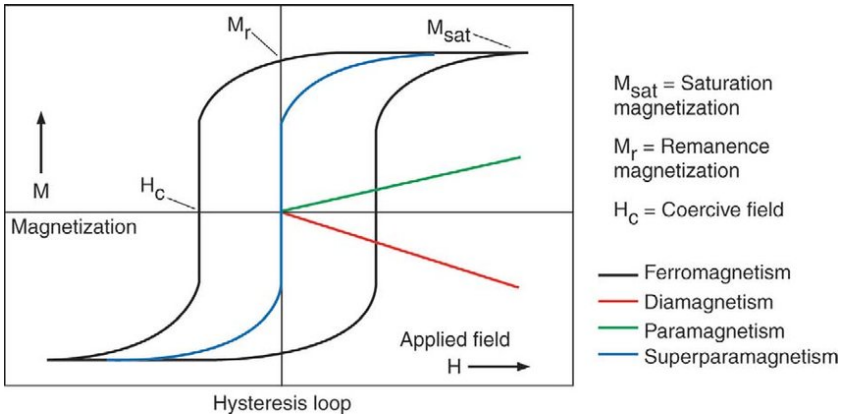

Figure 1.3: Hysteresis loop for ferromagnetic and superparamagnetic nanoparticles [35].

Figure 1.3 shows that ferromagnetic materials exhibit coercivity, meaning that they resist changes in the intensity of the external magnetic field. Therefore, particles with a diameter larger than a few tens of nanometers show resistance when changing the magnetic field, which strongly harms the SLP value.

The second reason that too large particles harm the heating efficiency is that large nanoparticles also have a lower surface-to-volume ratio, which also decreases the heat transfer efficiency.

Thirdly, the hysteresis area of SPIONs relies on the Néel and Brownian relaxation under an alternating magnetic field. The effective relaxation time (τ_{eff}) depends on both the Néel (τ_N) and Brownian (τ_B) relaxation processes, as presented in Equation 1.4.

$$\frac{1}{\tau_{\text{eff}}} = \frac{1}{\tau_N} + \frac{1}{\tau_B} \tag{1.4}$$

Equation 1.5 gives the parameters involved in the Néel relaxation process.

$$\tau_N = \tau_0 \exp\left(\frac{KV}{k_B T}\right) \tag{1.5}$$

Here, τ_0 is the characteristic attempt time, K is the magnetic anisotropy constant, V is the volume of the nanoparticle, k_B is the Boltzmann constant and T is the temperature.

Equation 1.6 gives the parameters involved in the Brownian relaxation process.

$$\tau_B = \frac{3\eta V_h}{k_B T} \tag{1.6}$$

Here, η is the viscosity of the surrounding medium, V_h is the hydrodynamic volume of the nanoparticle and once again is k_B the Boltzmann constant and T the temperature.

In the case of smaller nanoparticles (up to 15 nm), the Néel relaxation is dominant, for larger particles (larger than 15 nm) the Brownian relaxation is dominant [18]. In the case of Néel relaxation, the heat is generated by the energy loss produced by the rotation of the individual magnetic moment within the particle. In the case of Brownian relaxation, the heat is generated by the energy loss produced by the physical rotation of the entire particle itself. The Brownian relaxation time is linearly related to the viscosity of the liquid containing the particles and their hydrodynamic size. The TME heavily influences these two parameters, which can reduce the heating efficiency by up to 70-90% compared to an aqueous solution [18]. The Néel relaxation is less heavily influenced by these parameters, and therefore, the heating efficiency is less reduced in the TME. Therefore, a diameter up to 15 nm is desired since it relies on Néel relaxation. The fourth reason too large nanoparticles are undesirable is that injecting larger nanoparticles triggers inflammatory responses quicker, which strongly decreases the biocompatibility [36].

The second requirement regarding the size of the nanoparticles is that the distribution of the diameters should be as narrow as possible. The size of the particle heavily influences the magnetic hyperthermal effects as described before. An uneven distribution of nanoparticles can therefore induce uneven heating effects in tissue, which is highly undesirable considering the patient's safety.

1.7. Scope and outline of the thesis

As mentioned in Section 1.6.1, the SLP of the MNP is directly related to the shape, effective size and material properties of the MNP. However, to determine the dose of MNP and location of the injection of the MNPs in a tumour in order to achieve magnetic hyperthermia, it is of utmost importance to have a thorough understanding of the heating properties of these MNP. Ideally, one could have MNP that are only display the desired heating response in the TME, so that the impact on healthy tissue is minimised. It is hypothesised that this can be achieved with iron oxide nanoparticles with a cysteine coating. However, it is yet unknown what the effect of various GSH concentrations are on cysteine coated nanoparticles and how these concentrations influences the heating efficiency.

This thesis aims to answer the following research question *'How does the TME-biomarker GSH influence the magnetic hyperthermal properties of MNP for thermo-brachytherapy to treat early-stage breast cancer?* To answer this research question, first, the MNP surface chemistry was altered with cysteine. Secondly, the initially monodispersed, aggregated (after the addition of hydrogen peroxide) and once again redispersed (after the addition of GSH) were analysed with FTIR, DLS and TEM. Thirdly, the magnetic hyperthermal properties of these samples were analysed by measuring the temperature increase in the presence of an alternating magnetic field. It was hypothesised that lower concentrations of GSH (as in healthy tissue) would lead to aggregation and higher concentrations (as in the TME) would lead to dispersion. Therefore, it can be expected that these coated nanoparticles generate heat more efficiently in the TME and thereby limit the thermal damage to healthy tissue. An important aspect in this context is the possible diffusion of MNP from the injection point. This process was modelled and the effect of such diffusion on the heat distribution in the tumour was analysed in order to determine the dose and number of injection required to achieve magnetic hyperthermia.

2

Materials and Methods

Iron(II) chloride tetrahydrate was ordered from Sigma-Aldrich, Iron(III) chloride hexahydrate from Merck, Ammonium hydroxide solution with 25% NH_3 basis from Honeywell, L-cysteine from Sigma-Aldrich and Hydrogen peroxide (30%) from VWR Chemicals. To adjust the pH of suspensions, hydrogen chloride and potassium hydroxide from Sigma-Aldrich were used. For the destruction of the particles for ICP-MS, 90% nitric acid from Sigma-Aldrich was used. For the synthesis of the ZIF-8 frameworks, 99.8% methanol, zinc nitrate hexahydrate and 2-methylimidazole from Sigma-Aldrich were used.

2.1. Preparation of iron oxide nanoparticles

The synthesis was performed using the co-precipitation method inspired by Fadli et al. [37] and Sangeetha et al. [38]. Iron(II) chloride tetrahydrate and iron(III) chloride hexahydrate were combined at a 1:2 ratio in MilliQ. This solution is continuously stirred at 1000 rpm for 10 minutes in a water bath at 70°C to ensure the iron ions are completely dissolved. Ammonium hydroxide was diluted with MilliQ to 10% and added dropwise to the iron solution while maintaining continuous stirring and a temperature of 70°C. Ammonium hydroxide was added until the pH value reached 8.7, after that, the suspension was stirred for 20 more minutes at 70°C.

After cooling the suspension down, it was centrifuged at 11.000 rpm for 8 minutes and the supernatant (containing remaining ions, ammonium and excess solvent) was removed. The nanoparticles were cleaned three times by resuspending the pellet in MilliQ, centrifuging the suspension and removing the supernatant. The suspension was then centrifuged for 8 minutes at 2.000 rpm to remove the largest particles, after which only the supernatant was taken.

An approximation of the nanoparticle concentration was made by taking an Eppendorf containing 500 µL of the cleaned nanoparticle solution and measuring the weight of the Eppendorf before and after drying the suspension at 60°C for 24 hours. After this approximate concentration was determined, the nanoparticle solution was diluted to 5 mg/mL.

2.1.1. Treatment for the cysteine-based method

25 mg/mL L-cysteine was added to the nanoparticle solution of 5 mg/mL based on the research of Sangeetha et al. [38]. The suspension was then cleaned three times using centrifugation at 11.000 rpm for 8 minutes and magnetic decantation. Hydrogen peroxide was added to a final concentration of 0.2M. The suspension was once again cleaned three times using centrifugation at 11.000 rpm for 8 minutes and magnetic decantation. GSH was added to a final concentration of either 3 µM, 10 µM or 10 mM. The GSH was not removed before analysis.

2.1.2. Treatment for the ZIF-8-based method

The zeolitic imidazolate framework-8 (ZIF- 8) encapsulation method was based on the research of Wu et al. [39]. 3 mL of 5 mg/mL nanoparticles was centrifuged after which the supernatant was replaced by methanol. The nanoparticles were diluted in 30 mL methanol. This suspension was sonicated for

20 minutes. 1.23g 2-methylimidazole was dissolved in 10 mL methanol and added to the nanoparticle suspension, which was then sonicated again for 15 minutes. 0.56g of zinc nitrate hexahydrate was dissolved in 10 mL of methanol and combined with the nanoparticle suspension. The solution was stirred continuously at room temperature at 1000 rpm for 24 hours. Afterwards, the solution was left to dry for another 24 hours at 60 °C.

To the Fe_3O_4@ZIF-8 particles, either 3 µM GSH at pH 7.5 or 10 µM GSH at pH 6.5 was added. These two conditions represent the healthy tissue and the TME respectively. The samples were incubated at room temperature while stirring for 3 hours before they were analysed.

2.2. Surface and size analysis

DLS was used to analyse the size and accumulation of the nanoparticles. The laser had a wavelength of 632.8 nm and the scattering was measured at 90 degrees. For each measurement, the sample was analysed for 30 seconds. For the size distribution analysis in the ALV5000W software, the unweighted radius was taken into account. Based on the TEM images, a size distribution was obtained by using the software ImageJ.

2.3. Magnetic hyperthermal analysis

The magnetic hyperthermal properties of the magnetic nanoparticles were analysed using the magneTherm Digital from nanoTherics with a coil module of 60 mm. An alternating frequency of 338 kHz [40], a magnetic flux density of 18 mT [41] and an exposure time of 5 minutes were used, which are all declared patient-safe in the Netherlands. Before starting the measurement, a temperature variation of 0.5°C was allowed in one minute. The device contained two probes to measure the temperature. One of these probes was positioned in the upper part of the sample, the other probe at the bottom of the Eppendorf tube. This way, in case the sample was not well-dispersed but precipitated, the temperature in both the supernatant and the precipitate could be measured.

In the case of the magneTherm Digital software, the SLP was calculated with Equation 2.1.

$$\text{SLP} = \frac{\Delta T \cdot C_p}{m \cdot \Delta t} \tag{2.1}$$

Here, ΔT represents the measured change in temperature (K or °C), C_p the specific heat capacity of the solvent (water) ($\text{J} \cdot \text{mg}^{-1} \cdot \text{K}^{-1}$), m the mass of the nanoparticles (mg), and Δt indicates the change in time (s).

Each sample contained 1 mL with a weighted concentration of 5 mg/mL nanoparticles. The concentration of these suspensions after heating was verified using ICP-MS and the calculated SLP value was adjusted accordingly. The nanoparticles were first degraded to ions by adding 25 µL of the nanoparticle suspension to 500 µL of 65% nitric acid. Based on the assumption that the suspension has a concentration of 5 mg/mL nanoparticles, the suspension was further diluted to a concentration of 100 µg/L using 1% nitric acid before performing ICP-MS. For the ICP-MS, NexION2000 produced by PerkinElmer was used (helium profile, atomic weight 56 and 57).

3

Results and Discussion

In this thesis, the goal was to examine the effect of GSH on the magnetic hyperthermal properties of MNP. The iron oxide nanoparticles were first synthesised, characterised with DLS, FTIR and TEM and the heating efficiencies were measured and compared. The diffusion of the nanoparticles was modelled and the effect of the diffusion on the heating distribution analysed. Finally, another method was proposed in order to achieve (partially) selective heating of the tumour.

3.1. Preparation of the iron oxide nanoparticles

The iron oxide nanoparticles were synthesised using co-precipitation. These particles were cleaned and diluted to 5 mg/mL (22 mM). L-cysteine was then added to a final concentration of 25 mg/mL (206 mM). This caused the molar ratio between the nanoparticles and the cysteine to be 1:9.5. This ratio was chosen based on the research of Sangeetha et al. [38], since a similar concentration in their research resulted in the most stable nanoparticles. After incubation with cysteine and cleaning, the particles were incubated with 200 mM hydrogen peroxide and cleaned once again. This concentration was chosen didactically, keeping in mind that the hydrogen peroxide concentration should ideally be just under 10 times the concentration of bound cysteine [42]. Finally, GSH was added to a final concentration of either 3 µM, 10 µM or 10 mM. These GSH concentrations represent the extracellular GSH concentration around healthy cells, around cancer cells and the intracellular concentration of tumour cells respectively.

Samples were taken directly after synthesis, after adding cysteine, after adding hydrogen peroxide and after adding GSH. These samples were all analysed using DLS, FTIR and TEM in order to evaluate the size distribution and to characterise the surface.

3.2. Characterisation with DLS

DLS was used to analyse the hydrodynamic radius of the particles. The hydrodynamic radius is not only influenced by the physical diameter of the nanoparticles itself but also by the surfactants and the distribution of the particles. These surfactants interact with the nanoparticles through for instance ionic interactions. Figure 3.1 presents the distribution of the hydrodynamic radii (R_H) of the nanoparticles after synthesis, after the addition of cysteine (Cys), after the addition of hydrogen peroxide and after the addition of 10 µM GSH.

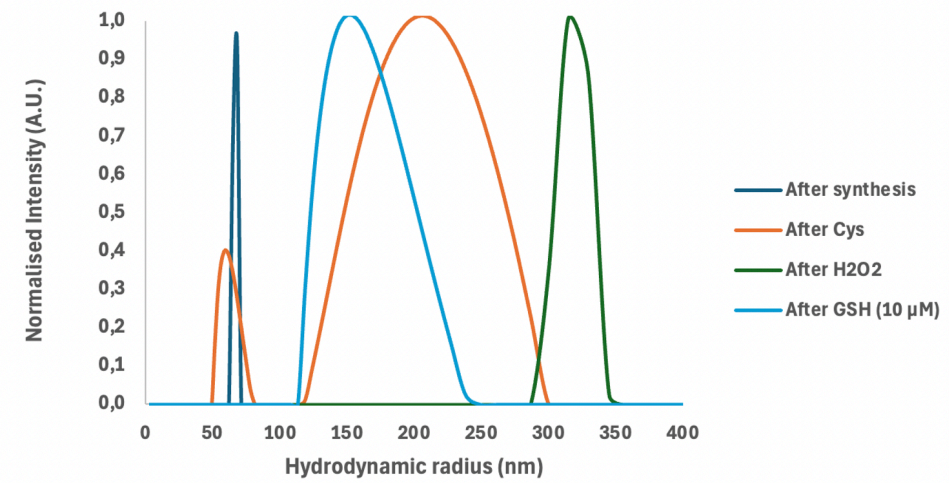

Figure 3.1: Hydrodynamic radii (nm) of the nanoparticles after synthesis, after addition of cysteine, after addition of hydrogen peroxide and after addition of 10 µM GSH. The intensities on the y-axis are normalised. R_H, after synthesis = 67 nm, R_H after Cys,1 = 64 nm, R_H, after Cys,2 = 209 nm, R_H, after H_2O_2 = 323 nm,R_H, after 10 µM GSH = 172 nm.

In Figure 3.1, only the peaks smaller than 1 µm were taken into account. This is done since a sample containing only MilliQ water, which should give no peaks at all, gave a background signal resulting in peaks around a few µm in all samples. This background signal is most likely due to contamination with bacteria or dust. Due to time constraints, it was not possible to remove this contamination using filtration for instance. It would be strongly suggested to perform this filtration in future research before performing DLS.

The following can be concluded from Figure 3.1. The nanoparticles after synthesis, so without any coating, had a mean hydrodynamic radius of 67 nm. The width of the peak is relatively narrow, which indicates that the variation in particle size is minimal.

After the addition of cysteine, DLS resulted in two peaks. The first peak could represent the uncoated nanoparticles since the hydrodynamic radius is just slightly smaller than the radius of the nanoparticles after synthesis. Another explanation could be that these particles are cysteine molecules that are bound to each other, forming large cysteine clusters. The second peak might represent nanoparticles with a larger hydrodynamic radius, which could indicate that the nanoparticles are coated with cysteine. Another explanation could be that the nanoparticles aggregated slightly, and therefore the total hydrodynamic radius is much higher. It can also be seen that these nanoparticles vary relatively in their size.

After the addition of hydrogen peroxide, the radius increases even more. This could once again indicate that hydrogen peroxide interacts with the nanoparticles and therefore increases the radius or that hydrogen peroxide causes aggregation, possibly by inducing disulfide bonds. The peak around 64 nm is not visible anymore, which strongly favours the aggregated cysteine explanation for this peak rather than the uncoated nanoparticles.

Finally, when 10 µM GSH is added, the hydrodynamic radius lowers significantly to a radius even lower than after cysteine addition. This could indicate that the disulfide bonds between the cysteines are broken, and therefore the nanoparticles are less aggregated.

However, it is of utmost importance to note that the data derived from DLS was somewhat variable. While the pattern in the peaks was mostly consistent, the exact hydrodynamic radii varied. Therefore, one should be rather cautious to draw conclusions solely based on these DLS results.

3.3. Characterisation with FTIR

FTIR analyses the molecular composition of the samples. In this thesis, FTIR was used to analyse the presence of thiol and disulfide groups on the nanoparticles. FTIR was performed with GSH, cysteine

and the nanoparticles in various conditions, see Figure 3.2.

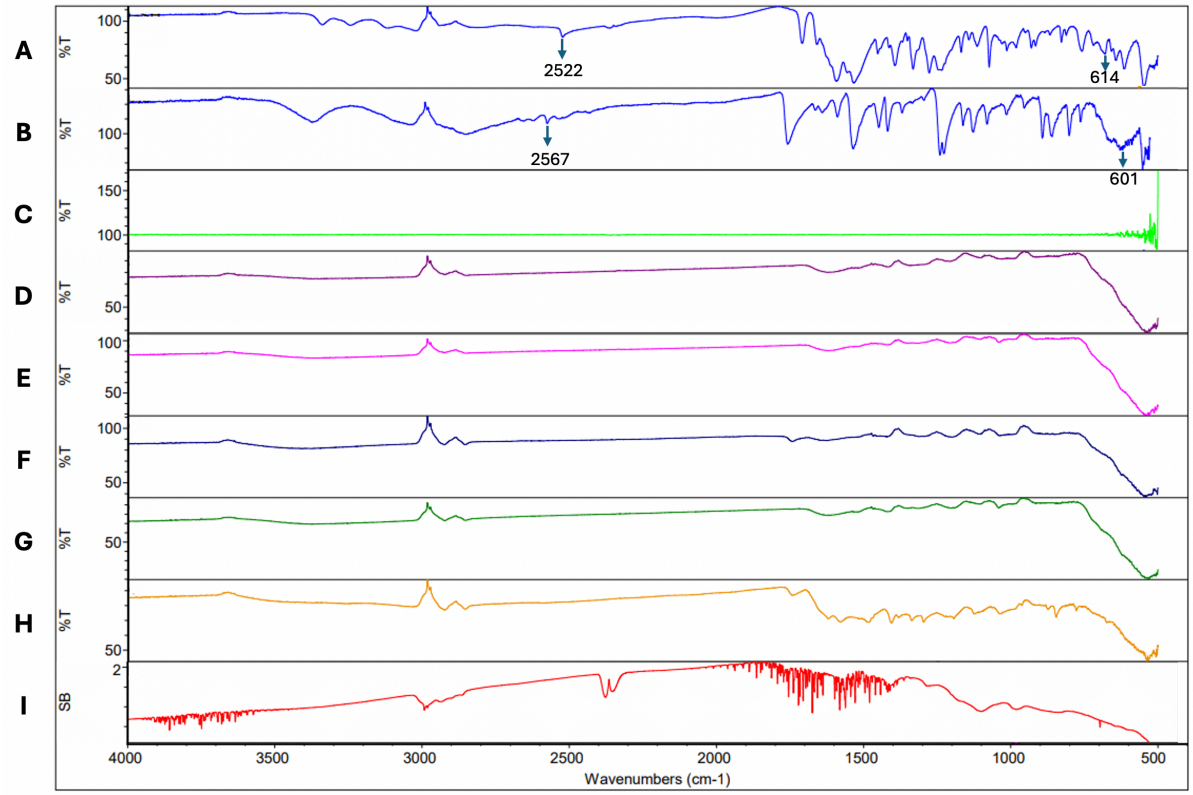

Figure 3.2: FTIR spectrum of various samples. **A)** Pure GSH. **B)** Pure cysteine. **C)** Nanoparticles after synthesis. **D)** Nanoparticles after cysteine. **E)** Nanoparticles after H_2O_2. **F)** Nanoparticles after 3 µM GSH. **G)** Nanoparticles after 10 µM GSH. **H)** Nanoparticles after 10 mM GSH. **I)** Background signal. All peaks in the disulfide region (S-S stretch) (600-620 cm^{-1}) and thiol region (S-H stretch) (2550-2600 cm^{-1}) were annotated.

In Figure 3.2, only 2 samples contained peaks in the thiol region (2550-2600 cm^{-1}) and disulfide region (600-620 cm^{-1}), namely the pure GSH and cysteine. Cysteine and GSH were only expected to have peaks in the thiol region. The disulfide peaks can be explained by spontaneous disulfide bond formation with the oxygen as an electron acceptor [43]. All the samples containing cysteine-coated nanoparticles were expected to have peaks in either the thiol or disulfide regions. Ideally, one should see that the sample with the nanoparticles after cysteine had peaks in the thiol region and after the addition of hydrogen peroxide mainly in the disulfide region. Increasing the concentration of GSH should give an increasing ratio between the thiol peaks compared to the disulfide peaks. The absence of peaks in either of these two regions in the samples with the nanoparticles can have one of the following two reasons. First of all, it could be possible that the background signal was too strong compared to the other samples. This could be the case if the grid on which the samples are analysed is contaminated. Since the background signal is subtracted from the signal of the samples, it might be that this causes the remaining signal to be too weak to be able to identify peaks. A second explanation might be that the mass of the samples with the nanoparticles was too small to obtain a strong signal. The amount of analysed GSH and cysteine was slightly larger, and since those signals gave satisfactory results, this explanation can be considered reasonable. It is most likely that a combination of these explanations is the most accurate. Since the background signal was too strong, large quantities of the samples were necessary.

Either way, the FTIR results were not adequate to conclude anything regarding the thiol/disulfide ratio in the samples. It is strongly recommended to perform the FTIR again in future studies with a higher amount of sample and cleaning the grid thoroughly beforehand. Unfortunately, this was not possible within the scope of this thesis due to time constraints.

3.4. Characterisation with TEM

TEM was performed as well in order to determine the physical diameter and the aggregation states of the particles in various conditions. Figure 3.3 displays the obtained TEM images of the particles after synthesis, after cysteine addition, after hydrogen peroxide addition and after addition of 10 µM GSH.

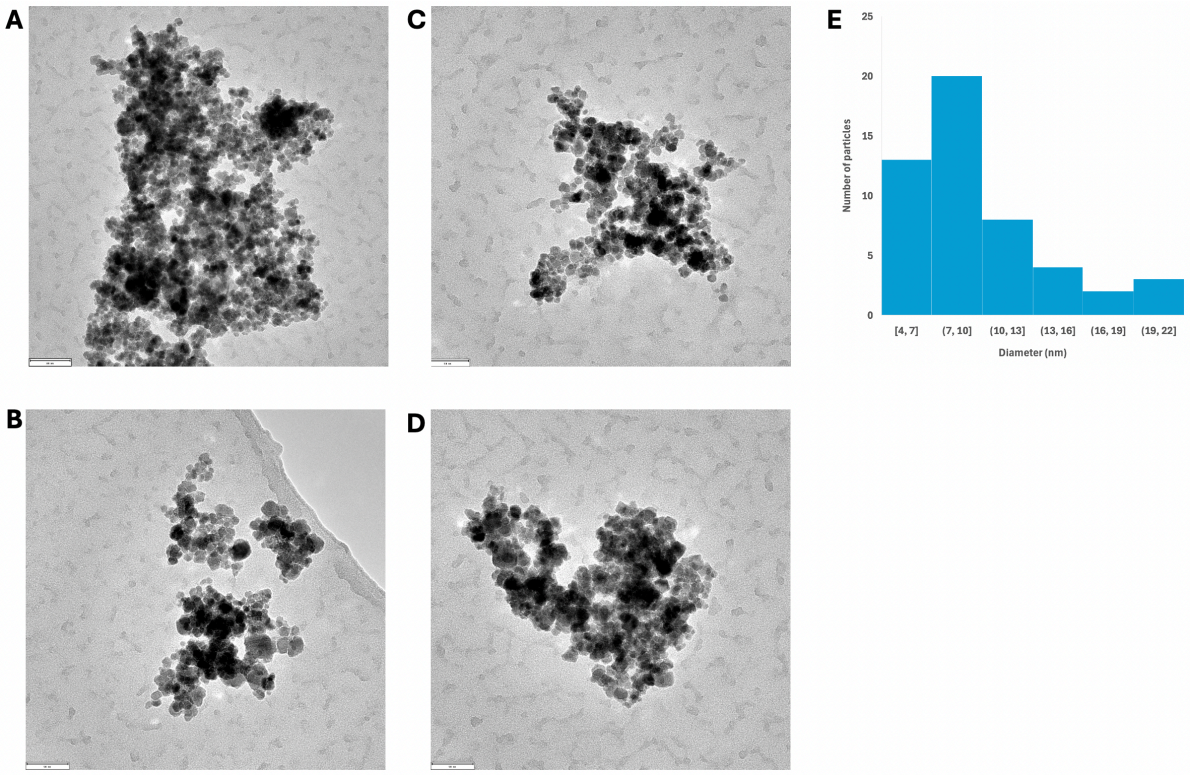

Figure 3.3: TEM images of the nanoparticles in different conditions. **A)** Nanoparticles after synthesis with a scale is 60 nm. **B)** Nanoparticles after Cys addition with a scale is 50 nm **C)** Nanoparticles after hydrogen peroxide addition with a scale is 50 nm. **D)** Nanoparticles after 10 µM GSH addition with a scale is 50 nm. **E)** Size analysis of particles in Figure A. Mean diameter is 10.1 nm (with standard deviation of 4.0 nm)

The main result achieved from Figure 3.3 is the acquired information about the size distribution. In order to use these particles for a safe thermo-branchy treatment, the particles had two requirements regarding their size. First of all, as mentioned in Section 1.6.1, the particles should be around 13-15 nm. The mean diameter of 10±4 nm was determined based on the diameter of 50 particles in Figure 3.3.A. The particles in Figure 3.3.A to 3.3.D are all comparable in size, but all slightly smaller than this optimal diameter. For future research, it is advised to decrease the concentration of the added ammonium hydroxide (e.g. 5% instead of 10%) to achieve slightly larger nanoparticles [44]. The ammonium stabilises the synthesised particles and therefore inhibits a further increase of the diameter. Therefore, a lower ammonium concentration allows for larger nanoparticles.

A second requirement regarding the size of the particles was that the size distribution should be as narrow as possible. As the standard deviation of the diameter of the particles was 4.0 nm, the distribution is not quite narrow yet. A way to combat this for future research is to sort the particles with the use of varying rotational forces during centrifugation, as is done by Dadfar et al. [45]. The distribution was expected to follow a normal distribution, however, one can see that there are more particles with a diameter smaller than the mean diameter. This can be explained by critically analysing the cleaning method of these particles. Large particles were mainly removed by taking the supernatant after centrifuging the particles at 2.000 rpm for 8 minutes. The smaller particles could were removed when taking the pellet after centrifuging the particles at 11.000 rpm for 8 minutes, but it is much more likely that these were present in the pellet as well (supernatant was colourless).

When analysing the particles after synthesis, the difference between the mean diameter of 10±4 nm

found using TEM and the mean hydrodynamic radius of 67 mm and thus a diameter of 134 nm using DLS is quite large. This could be explained by the fact that DLS measures the hydrodynamic radius, and therefore takes into account not only the actual radius but also all molecules that are bound to the surface or interact with the surface. Another explanation could be that the particles after synthesis are aggregated, which causes DLS to recognise the aggregation of many particles as one large particle.

Ideally, one would see monodispersed particles in Figure 3.3.A, 3.3.B and 3.3.D and aggregated particles in 3.3.C. However, Figure 3.3 all show somewhat aggregated particles. This most likely is caused by the way the nanoparticles are prepared for TEM. A droplet of nanoparticle suspension in water was put on the TEM grid. As the water evaporates, the concentration of nanoparticles increases, which can lead to more attracting inter-particle forces. Therefore, drying the samples might not accurately represent the dispersion of the particles. A way to combat these drying effects might be to wash the grids with ultrapure water which induces a more uniform drying process [46]. Another way of combating this effect is by using environmental Scanning Electron Microscopy or Atomic Force Microscopy to analyse the nanoparticles in suspension directly.

3.5. Analysing the magnetic hyperthermal properties

The final goal of this thesis was to determine the effect of GSH on the magnetic hyperthermal properties of cysteine-coated nanoparticles. Therefore, the particles in different conditions were exposed to a magnetic field of 18 mT with an alternating frequency of 338 kHz. The SLP was calculated based for each of these conditions, see Figure 3.4

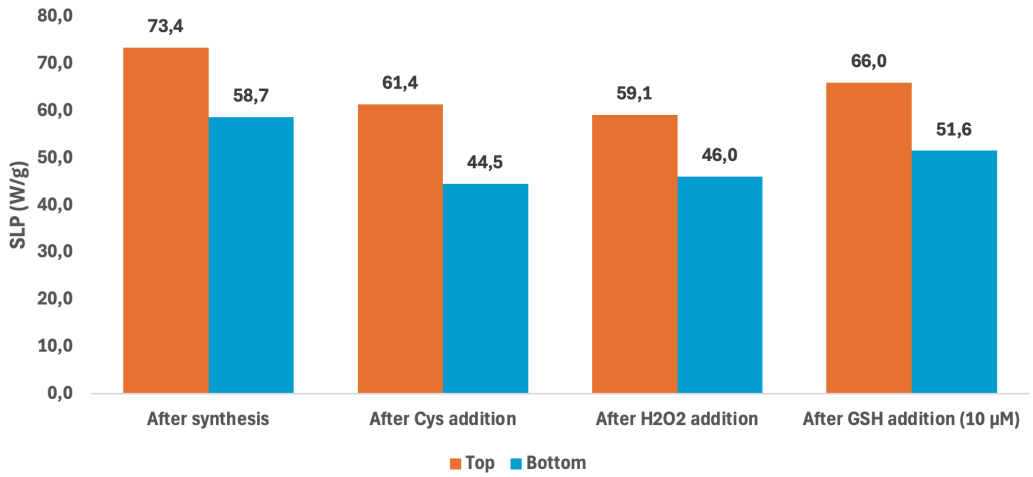

Figure 3.4: Graph of the calculated SLP values (W/g) of the nanoparticles after synthesis, after addition of cysteine, after addition of hydrogen peroxide and after addition of 10 µM GSH. The left bar ('Top') represents the probe in the upper part of the Eppendorf, the right bar ('Bottom') the probe in the lower part of the Eppendorf.

One can see in Figure 3.4 that the temperature change and therefore the SLP value derived from the upper probe is higher in all four conditions. This is to be expected in a well dispersed sample, since the bottom probe is closer to the cooling system and therefore the sample is cooled more around the bottom probe. When comparing various conditions, the SLP value derived from the upper probe is taken. All samples in this thesis were expected to have a standard deviation around 0.7 W/g. This standard deviation was determined by measuring the temperature difference in two samples in duplo and taking their average standard deviation. For future research, it is strongly recommended to calculate the standard deviation for each sample individually.

A conclusion that can be derived from Figure 3.4 is that the SLP value decreases when cysteine is added (decrease of 20%) and when hydrogen peroxide is added (decrease of 4%). This was expected, since it was hypothesised that these particles (partially) aggregated after the addition of cysteine and hydrogen peroxide.

While larger individual nanoparticles result in higher SLP values, aggregation of nanoparticles lowers

the SLP value of the sample [18]. If the particles aggregate, the magnetic core diameter does not increase, while the number of magnetic cores does. When comparing nanoparticles and nanoclusters (aggregated nanoparticles), nanoclusters tend to have lower SLP values than individual nanoparticles as was shown in Monte-Carlos simulations [47] and in practical experiments [48]. This is for the following two reasons. Individual nanoparticles can rotate more freely and therefore respond individually to an alternating magnetic field, which causes them to generate more heat [32]. Secondly, individual particles have less magnetic or dipole interactions with each other. Dipole interactions between particles has also been proven to have a negative effect on the relaxation time and therefore SLP values [49].

A second conclusion that can be drawn from Figure 3.4 is that the addition of 10 µM GSH causes the SLP to slightly increase with 11%. This slight increase in SLP could indicate that this concentration of GSH causes the nanoparticles to disperse slightly more.

In ongoing phase I and phase II clinical trials, an alternating magnetic field frequency of 100 kHz has mainly been used [50]. While a lower frequency allows for lower magnetic flux density (lower than the 18 mT used in this research). So while 338 kHz has been declared patient-safe, it might be interesting to analyse the heating effects at 100 kHz as well. Most likely, this will result in lower heating efficiency.

It was expected that the encountered differences in hydrodynamic diameter from Figure 3.1 in Section 3.2 and heating efficiencies from Figure 3.4 after the addition of hydrogen peroxide and GSH would be caused by the oxidation of the thiol groups and reduction of the disulfide groups respectively. However, it was not proven that the encountered changes in hydrodynamic diameter and heating efficiency were caused by these oxidisation and reductions themselves. For future studies, it is of utmost importance to first study this reaction, possibly even without the presence of nanoparticles as a proof of concept. This could be done by taking cysteine, cysteine incubated with hydrogen peroxide and cysteine incubated with GSH. While FTIR gave little quantitative insights, HPLC, MS or NMR can be used to determine the ratio between the free thiol groups and disulfide bonds between the cysteines. Another method to determine the amount of free thiol groups in a sample is with Ellman's Test. In this test, the 5,5'-dithiobis(2-nitrobenzoic acid) (DTNB) reagent reacts with free thiols to produce a yellow-colored product, which can be quantified by measuring absorbance at 412 nm. Measuring the thiol/disulfide ratio could show that the difference in heating efficiencies is truly caused by the oxidation and reduction of cysteine. Another possibility to prove that GSH truly reduced the disulfide bond is by measuring the GSH/GSSH ratio. It is expected that the GSSH concentration is higher after the reduction of the disulfide bonds between the cysteines. This ratio can either be determined with HPLC, MS, NMR or with the use of a GSH/GSSH detection kit [51].

If it was assumed that the difference in heating efficiencies was indeed caused by the oxidation and reduction of the thiol groups and the disulfide bonds of the cysteines, it is not suprising that the addition of GSH causes only slightly increases (11%). This mechanism relies on the thiol-disulfide exchange between cysteine and GSH. However, the dissociation constant (pKa) of GSH is 9.2 and of cysteine 8.3 [52]. At pH values lower than 9.2, GSH mainly contains a thiol group and at pH values higher than 9.2, GSH mainly contains a thiolate group (deprotonated thiol). At pH 7.5, the ratio between the thiolate and thiol is 0.02, at pH 6.5 this ratio lowers to 0.002. Since the thiol-disulfide exchange between the cysteine and GSH requires GSH to have a thiolate group, the exchange rarely happens at pH 7.5 or 6.5. Because of this low exchange efficiency, it was expected that the addition of GSH only induced a small difference in heating efficiency.

3.6. Effect of the GSH concentration

During this thesis, different GSH concentrations were analysed as well. The aforementioned results are achieved with a GSH concentration of 10 µM, which falls in the range of the extracellular GSH concentration near cancerous cells (2-10 µM) [12]. The extracellular concentration near healthy cells is around 2-4 µM [11]. Therefore, this experiment was repeated at a GSH concentration of 3 µM as well to compare the effect in the extracellular GSH concentrations near cancerous and near healthy cells. A concentration of 10 mM was also analysed, which falls in the range of the intracellular GSH concentrations in cancerous cells.

These three GSH concentrations were first analysed visually. See Figure 3.5

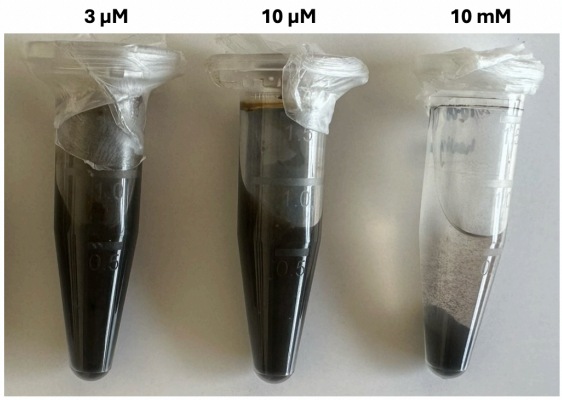

Figure 3.5: Photograph of Eppendorf tubes containing nanoparticles coated with cysteine after addition with 3 µM, 10 µM and 10 mM GSH after 15 minutes.

One can clearly see that the nanoparticles in 3 µM and 10 µM GSH concentrations are much more dispersed than the particles in a 10 mM GSH concentration. The particles in the 10 mM GSH concentration were more likely to precipitate. Secondly, the influence of these concentrations on the hydrodynamic radius was analysed. The results are presented in Figure 3.6.

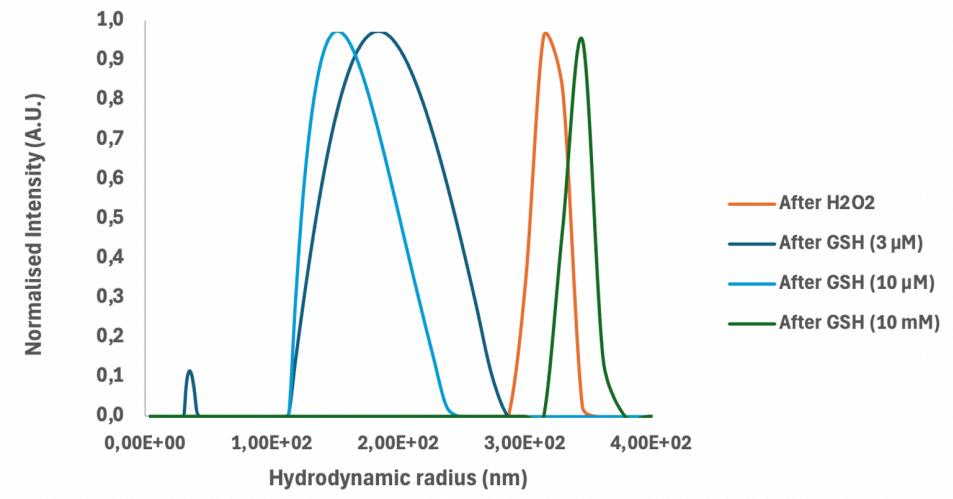

Figure 3.6: Hydrodynamic radii (nm) of the nanoparticles before and after addition of 3 µM, 10 µM and 10 µM GSH. The intensities on the y-axis are normalised. R_H, after H_2O_2 = 323 nm, R_H with 3 µM GSH,1 = 36 nm, R_H with 3 µM GSH,2 = 183 nm, R_H with 10 µM GSH = 172 nm, R_H with 10 mM GSH = 346 nm.

From Figure 3.6, the following can be concluded. After the addition of 3 µM GSH, the hydrodynamic radius decreases from 323 nm to 183 nm. The addition of 10 µM GSH caused the hydrodynamic radius to be even smaller than after the addition of 3 µM (172 nm). However, the addition of 10 mM did not cause a decrease in the hydrodynamic radius, but rather an increase to 346 nm.

Another peak of 36 nm was visible after the addition of 3 µM GSH, but it is very unlikely that these are nanoparticles as well. Most likely, these are aggregated GSH molecules. However, it is interesting that this peak is not present after the addition of 10 µM of 10 mM GSH. This peak was not present during all replicates of the measurement, which might be since these aggregated GSH molecules were present in low concentrations.

Based on these radii, it could be concluded that the addition of 3 and 10 µM reduced the aggregation of the nanoparticles, while 10 mM GSH caused the particles to aggregate even further. However,

once again, no reliable conclusions can be drawn solely from these results due to some variation in measurements.

The influence of the three GSH concentrations was also analysed using TEM, see Figure 3.7.

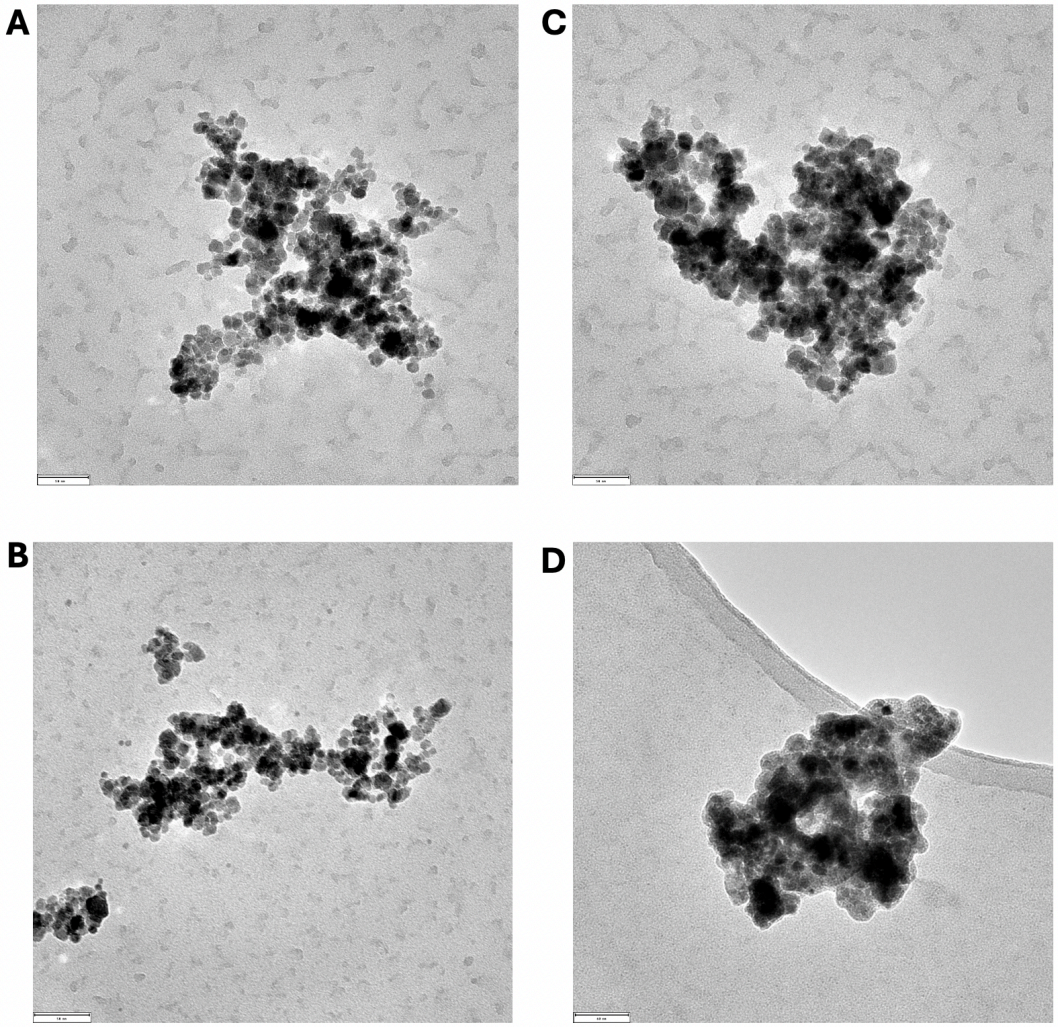

Figure 3.7: TEM images of the nanoparticles in GSH concentrations. **A)** Nanoparticles after hydrogen peroxide addition with a scale of 50 nm. **B)** Nanoparticles after 3 µM GSH addition with a scale of 50 nm. **C)** Nanoparticles after 10 µM GSH addition with a scale of 50 nm. **D)** Nanoparticles after 10 mM GSH addition with a scale of 60 nm.

Figure 3.7.A to Figure 3.7.C look quite similar regarding the size of the particles and their aggregation. However, it is quite interesting to see that the particles in Figure 3.7.D are not only aggregated but fused together as well. This indicates that a concentration of 10 mM GSH for this concentration of nanoparticles is too high for the particles to still be dispersed or slightly aggregated. It might be that this amount of GSH allows for too much interaction with the surface. This could have one of the following reasons.

The nanoparticles after synthesis have a pH of 8.7, after the addition of cysteine 6.7, after the addition of hydrogen peroxide 5.0 and after the addition of 10 mM GSH 4.4. Cysteine, at pH values between 2 and 8, is a zwitterion, see Figure 3.8.

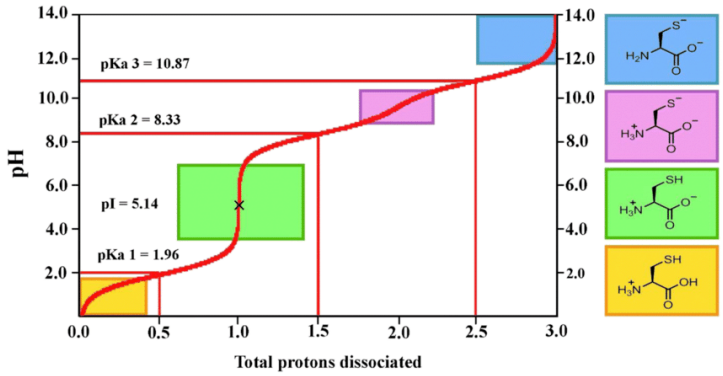

Figure 3.8: Net charge of cysteine at various pH values [53]

In this case, the functional groups of GSH could interact with the positively or negatively charged groups of cysteine and therefore link the particles together. Another explanation is that the change in pH caused by the addition of GSH, causes the particles to reduce their surface charge and therefore reduce the electrostatic repulsion between the particles. All of these explanations would promote aggregation and could potentially lead to a slight nanoparticle fusion after a certain period.

The heating efficiencies after the addition of 3 µM, 10 µM and 10 mM GSH were also analysed, see Figure 3.9

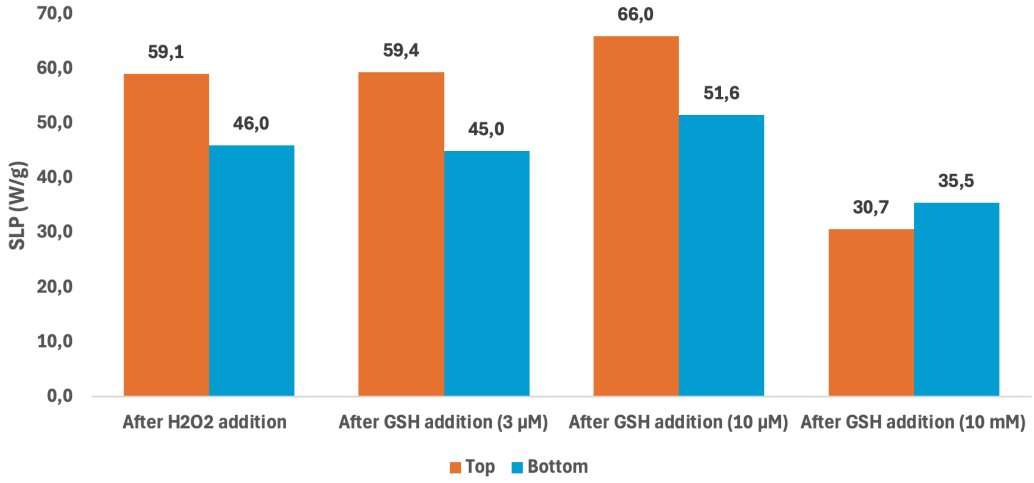

Figure 3.9: Graph of the calculated SLP values (W/g) of the nanoparticles after addition of hydrogen peroxide, after addition of 3 µM GSH, after addition of 10 µM GSH and after addition of 10 mM GSH. The left bar ('Top') represents the probe in the upper part of the Eppendorf, the right bar ('Bottom') the probe in the lower part of the Eppendorf.

Figure 3.9, shows that for all the samples, except for the sample with 10 mM GSH, the upper probe gave higher SLP values. This indicates that at 10 mM GSH, the nanoparticles had a stronger tendency to precipitate. This figure shows that the addition of 3 µM GSH increases the heating efficiency insignificantly (0.3 W/g). The addition of 10 µM GSH increases the SLP more (6.9 W/g), while the addition of 10 mM GSH decreases the SLP by (28.4 W/g). This figure therefore shows that the nanoparticles heat more efficiently (increase of 11%) in an environment with 10 µM GSH compared to 3 µM GSH. This indicates that the nanoparticles heat the TME more than healthy tissue, but only with a rather small difference in heating efficiency. This difference was further analysed in Section 3.8. If these nanoparticles are present in a 10 mM GSH environment, so inside a cancerous cell, the heating efficiency decreases steeply.

3.7. Effect of the pH after GSH addition

A pH analysis was performed as well to analyse the effect of the pH value on the heating efficiencies of cysteine-coated nanoparticles. This analysis was performed at a GSH concentration of both 10 µM and 10 mM.

3.7.1. After the addition of 10 µM GSH

After the addition of 10 µM GSH, four suspensions were made with pH values ranging from 5.5 to 8.5. None of these suspensions showed visible precipitation. The heating efficiencies of these four samples were analysed and presented in Figure 3.10.

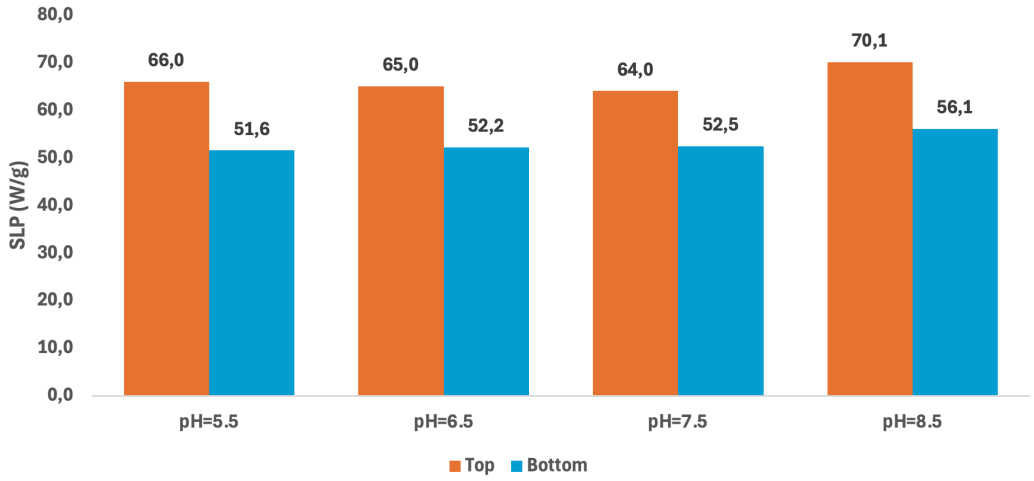

Figure 3.10: Graph of the calculated SLP values (W/g) of the nanoparticles after addition of 10 µM GSH and altering the pH to 5.5, 6.5, 7.5 and 8.5. The left bar ('Top') represents the probe in the upper part of the Eppendorf, the right bar ('Bottom') the probe in the lower part of the Eppendorf.

Figure 3.10 shows that the upper probe gave higher SLP values than the lower probe for all samples. This indicates that all four samples are well dispersed. The samples at pH values 5.5 to 7.5 all give somewhat similar SLP values. At a pH of 8.5, the SLP value is slightly higher, but no clear relation between the pH and obtained SLP values can be derived from this data. However, it was expected that higher pH values gave higher heating efficiencies since the thiol-disulfide exchange is more favourable at higher pH values. A possible explanation could be that the GSH concentration was much higher than the bound cysteine concentration, which resulted in enough thiolated GSH molecules to reduce all disulfide bonds between the cysteines.

3.7.2. After the addition of 10 mM GSH

The effect of the pH values was also analysed at a GSH concentration of 10 mM. Figure 3.11 shows the visual analysis.

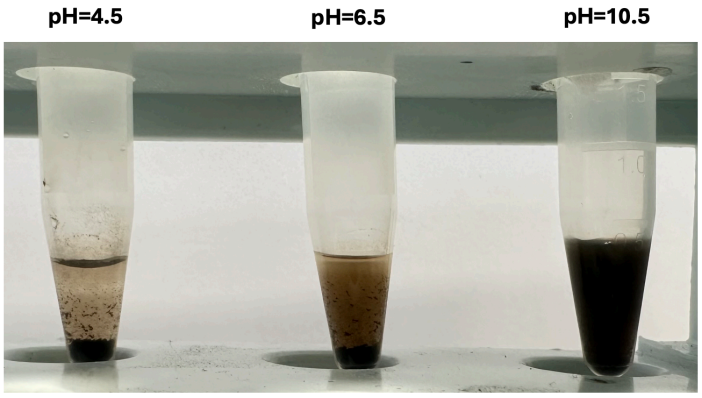

Figure 3.11: Photograph of Eppendorf tubes containing nanoparticles coated with cysteine after addition of 10 mM GSH at pH 4.5, 6.5 and 10.5

Figure 3.11 shows the following. The precipitation of the particles upon the addition of 10 mM GSH was encountered at pH 4.5 and 6.5. This was also seen at a pH value of 8.5, which was unfortunately not photographically captured in this research. However, the addition of 10 mM GSH did not have a precipitation effect at a pH 10.5. Also, the heating efficiencies of the nanoparticles after the addition of 10 mM GSH were analysed at pH 4.5, 6.5 and 8.5 and presented in Figure 3.12.

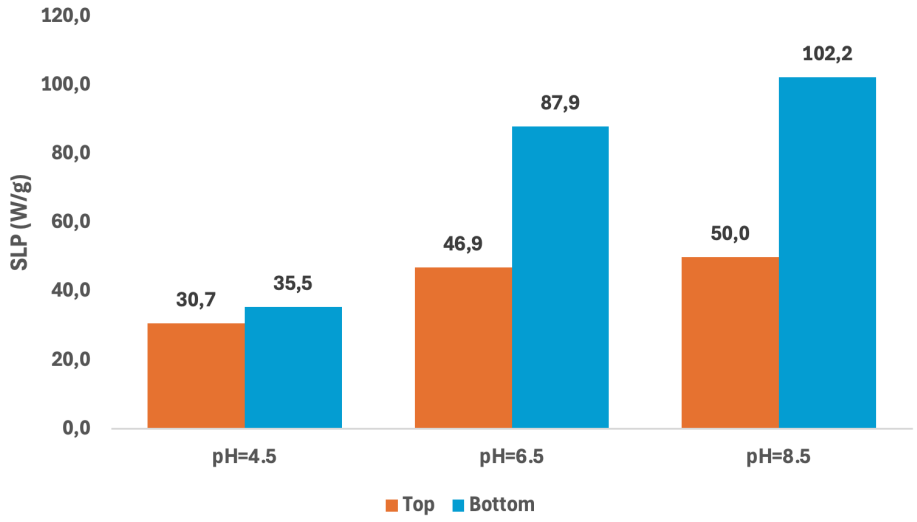

Figure 3.12: Graph of the calculated SLP values (W/g) of the nanoparticles after addition of 10 mM GSH and altering the pH to 4.5, 6.5 and 8.5. The left bar ('Top') represents the probe in the upper part of the Eppendorf, the right bar ('Bottom') the probe in the lower part of the Eppendorf.

It is interesting to see that the results in Figure 3.12, so at 10 mM GSH, vary significantly compared with Figure 3.10. At 10 mM, one can see that the lower probe gave higher SLP values for all pH values. This indicates that the nanoparticles all precipitated heavily, as was also visually established. Another clear difference between the GSH concentrations of 10 mM and 10 µM is that the samples with different pH values gave significantly different heating efficiencies at 10 mM. Figure 3.12 shows that the SLP values increase as the pH increases. At 10 mM SLP with a pH of 4.5 and 6.5, SLP values of 30.7 and 46.9 W/g were obtained. In the previous step, so after addition of hydrogen peroxide, the pH value was 5.0 and the SLP value 59.1 W/g (Figure 3.4). This SLP value is significantly higher than the SLP values after 10 mM GSH in the same pH range. Therefore, it can be concluded that the addition of GSH lowered the SLP value due to both the lower pH and the influence of GSH itself.

Based on these pH analyses, the following can be concluded. Differences in pH have a clear influence

on the precipitation and heating efficiencies upon the addition of 10 mM GSH. However, this difference was not significant upon the addition of 10 µM GSH. This indicates that the samples with a GSH concentration of 10 µM are less sensitive to pH differences.

3.8. Analysing the obtained heating efficiency

In case of hyperthermia, the tumour is heated to 44-46°C as mentioned in Section 1.3. If an average body temperature of 37°C is assumed, hyperthermia is achieved after a temperature difference of 8°C. To calculate how much energy would be needed to achieve this, Equation 3.1 can be used.

$$Q = m \cdot C_p \cdot \Delta T \tag{3.1}$$

In Equation 3.1, *Q* represents the heat energy in J, *m* the mass of the tumour in g, C_p the specific heat capacity of the tumour in J/(g K) and ΔT the desired temperature change (K or °C).

In the case of stage I tumours, the tumour is smaller than 2 cm [54]. So if a tumour diameter of 1 cm is assumed, and it is assumed that the tumour is spherical, the volume of the tumour would be 0.52 cm^3. Tumour tissue typically has a density of 1.079 g/cm^3 [55], which makes the mass of a tumour this size 0.56 g. The heat capacity of a malignant tumour is typically between 3.6 and 3.9 J/(kg K) [56]. So the required amount of heat energy for a 1 cm tumour, a heat capacity of 3.75 J/(kg K) and a temperature change of 8°C is 16.8 J. In order to calculate the required amount of nanoparticles, Equation 3.2 can be used.

$$SLP = \frac{Q}{t \cdot m} \tag{3.2}$$

Here, *t* represents the time the patient is exposed to the alternating magnetic field (exposure time), and *m* the mass of the nanoparticles used to achieve the heat change. So with a SLP value of 66.0 W/g (after addition of 10 µM GSH), a required heat energy of 16.8 J and an exposure time of 5 minutes, 0.9 mg of nanoparticles would be necessary. If the SLP value after addition of 3 µM GSH is 11% is lower, this amount of injected nanoparticles would give a 11% lower temperature change, so 7°C. This would indicate that if the tumour would be heated to 45°C, the healthy tissue would be heated to 44°C.

It is noteworthy that 44°C in normal tissue will enhance apoptosis and induce internucleosomal cleavage in DNA [57]. Therefore, it is crucial to find methods to increase the difference in SLP values of nanoparticles in healthy tissue and tumour environment.

3.8.1. Modelling the heat distribution

The increase in temperature in Section 3.8 does not take diffusion into account. However, this is not accurate since the nanoparticles might diffuse throughout the tissue upon injection. This causes the temperature increase to also depend on the distance from the injection site. To analyse the diffusion and how the diffusion alters the heating efficiencies throughout the tumour, a heat distribution model was proposed.

The diffusion was assumed to be one-dimensional. It was assumed that there would be one injection site exactly in the middle of a 1 cm tumour. The diffusion was simulated using the finite difference method. The tumour was divided into grids and the current concentration was calculated in each grid. If the concentration of a neighbouring grid was different, the nanoparticles diffused to the grid with the lower concentration with a diffusion rate depending on the concentration difference. Then, the concentration could be updated again according to Equation 3.3.

$$C_{n+1,i} = C_{n,i} + D_{\text{water}} \cdot \frac{\Delta x^2}{\Delta t} \cdot (C_{n,i+1} - 2 \cdot C_{n,i} + C_{n,i-1}) \tag{3.3}$$

Where, $C_{n+1,i}$ represents the concentration of nanoparticles at time $n+1$ and position i, $C_{n,i}$ the concentration of nanoparticles at time n and position i, D_{water} the diffusion coefficient of nanoparticles in water, Δx the distance between neighbouring grids, Δt the time step and $C_{n,i+1}$ and $C_{n,i-1}$ are the concentrations of nanoparticles at neighbouring grids $i+1$ and $i-1$ at time n, respectively.

However, to analyse how fast the particles can diffuse into a neighbouring grid, one should have knowledge on the diffusion coefficient of the nanoparticles in water (D_{water}). Based on Equation 1.1, the diffusion coefficient can be calculated based on the obtained hydrodynamic radius. When analysing the nanoparticles in TME, thus a concentration of 10 µM GSH, the obtained hydrodynamic radius was 172 nm (Figure 3.1). The diffusion coefficient is approximately $1.27 \cdot 10^{-12}$ m²/s assuming the temperature to be 298 K and the viscosity to be 0.001 Pa·s.

The concentration and mass distribution over time were calculated for 30 and 60 minutes, see Figure 3.13. Here, a dose of 0.9 mg in 90 µL (initial concentration of 10 mg/mL) was assumed.

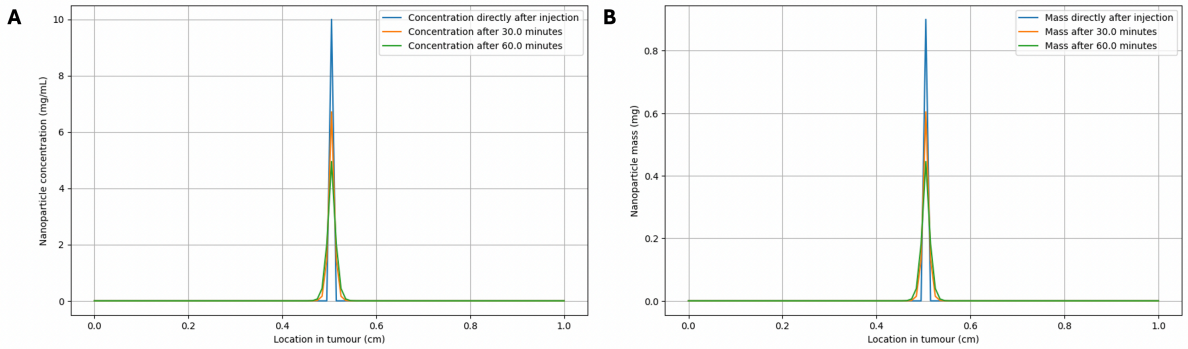

Figure 3.13: A) Modelled nanoparticle concentration over time. An initial concentration of 10 mg/mL in the middle of a 1 cm tumour is assumed. The concentration distribution after 30 and 60 minutes is displayed. **B)** Modelled nanoparticle mass over time. An initial mass of 0.9 mg in the middle of a 1 cm tumour is assumed. The mass distribution after 0, 30 and 60 minutes is displayed.

Figure 3.13 shows that even after an hour, the particles are mostly present within 250 µm of the original injection site. The diffusion rate is relatively low, which can be explained by the high hydrodynamic radius and thus the low diffusion coefficient.

To analyse the combined effect of the diffusion and the heating efficiency, a model of the temperature change over time at various distances from the injection site was made. In this model, the SLP value of the nanoparticles in a GSH concentration of 10 µM (66.0 W/g), a tumour mass of 0.56 g and a specific heat efficiency capacity of 3.75 J/(g K) were assumed once again. The temperature change was calculated using Equation 3.1 and Equation 3.2. The model is presented in Figure 3.14.

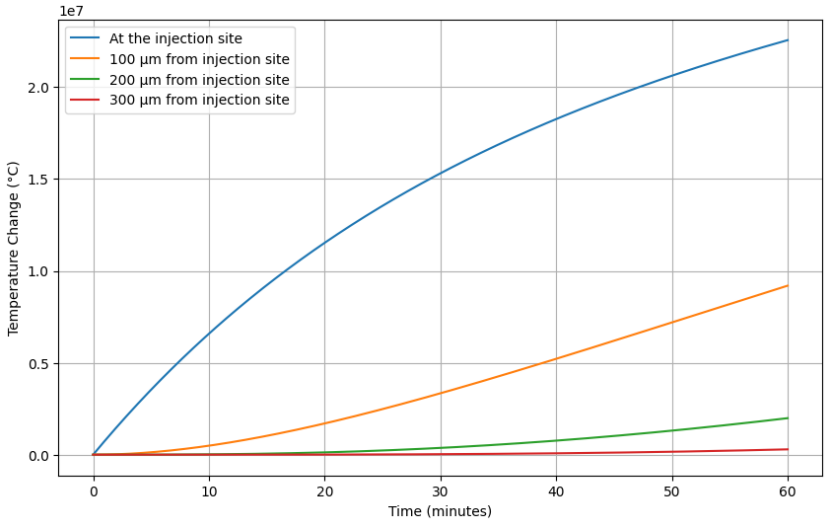

Figure 3.14: Accumulative temperature change over time at various distances from the injection site. An initial mass of 0.9 mg is used.

Figure 3.14 displays a significantly different temperature change after 5 minutes compared to the temperature change of 8°C in Section 3.5. One can see that at the injection site, the temperature change is $4 \cdot 10^6$ °C after 5 minutes. However, at merely 100 µm from the injection site, 5 minutes allows for a temperature change of $1.4 \cdot 10^5$ °C . These enormous temperature changes and large differences between the various distances from the injection site are both caused by the slow diffusion of the particles. Since they diffuse very slowly, many particles are still present at the injection site after 5 minutes, and almost none at 100 µm or further from the injection site.

So to conclude, the high hydrodynamic radius of the particles gives a low diffusion coefficient. This causes the nanoparticles to diffuse slowly and therefore causes the heating to be very local. Because of this, many injections would be needed, all with very low amounts of nanoparticles, which is undesired keeping the labour intensity in mind. Therefore, another requirement of the size of the nanoparticles is that the hydrodynamic radius of the particles should be as small as possible to allow particle diffusion as much as possible.

3.9. Alternative approaches

Based on the aforementioned SLP values at 3 µM GSH and 10 µM GSH and the derived calculations, achieving hyperthermia in the tumour environment would cause apoptosis in healthy tissue as well. Besides that, the large hydrodynamic radius necessitates multiple of injection sites. Therefore, this methodology requires many improvements prior to its application in magnetic hyperthermal therapy as a way to eradicate tumours. Because of this, it could be interesting to analyse other methodologies.

Another promising methodology to control the heating efficiency of the nanoparticles is by encapsulating the nanoparticles in a TME-responsive framework. Encapsulating the particles in a framework has an additional benefit, namely that the framework aids in the recovery of the particles. Having the particles collected in several larger frameworks prevents them from scattering individually and allows for more efficient recovery.

An example of this would be the metal-organic framework (MOF) ZIF-8. Encapsulated iron oxide nanoparticles in a ZIF-8 framework (Fe_3O_4@ZIF-8) can be relatively simply synthesised by combining a suspension with the nanoparticles and imidazole together with zinc nitrate. ZIF-8 is TME-responsive since its stability is highly dependent on the pH and GSH concentration of the environment. Previous literature suggests that a ZIF-8 framework can be completely dissolved when the GSH concentration is higher than 0.5 mM [58]. Also, a pH of 5 compared to 7.4 has been shown to increase the release of the substance it contains by approximately 40% [59]. Hoop et al. analysed the biocompatibility of ZIF-8 frameworks in human breast cell lines and found reduced cell viability to 80% after 72 hours at a ZIF-8 concentration of 30 µg/mL [60]. Higher concentrations gave drastically lower cell viabilities, which are caused by the released zinc ions which can influence the mitochondrial ROS production [60].

Another method to encapsulate the nanoparticles is with the use of a poly(d, l-lactide-co-glycolic acid) (PLGA) framework. These polymers have shown promising biodegradability and biological compatibility [61]. Encapsulated nanoparticles in PLGA can be synthesised by slowly adding a suspension containing the nanoparticles and PLGA to a solution with polyvinyl alcohol (PVA). Droplets of nanoparticles and PLGA are present in the PVA solution, after which the PLGA solidifies to obtain solid particles containing the nanoparticles. PLGA is also pH-responsive, and it has been shown to have a 12% higher release rate after 48h at a pH of 5.2 compared to 7.4 in the case of encapsulated curcumin [62].

It is hypothesised that both encapsulation methods would have the following effect. In the case of healthy tissue, so with higher pH values and lower extracellular GSH concentrations, the framework would be relatively dense or stable. This does not allow the nanoparticles to be released and therefore these encapsulated particles have a low heating efficiency. In the TME, so with lower pH values and higher extracellular GSH concentrations, the framework structure becomes less dense or slowly degrades causing the nanoparticles to be released. This release causes a higher heating efficiency. Therefore, the TME will be heated more than healthy tissue.

3.9.1. Results on ZIF-8 based method

Only the ZIF-8 based method was analysed on its heating efficiencies in conditions related to healthy tissue and to cancerous tissue. Two samples were compared. The first sample contained 3 µM GSH at

a pH-value of 7.5 and would represent healthy tissue. The second contained 10 µM GSH at a pH-value of 6.5. The heating efficiencies are presented in Figure 3.15.

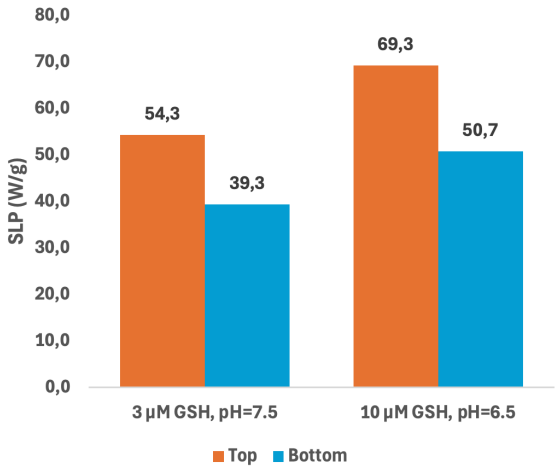

Figure 3.15: Graph of the calculated SLP values (W/g) of the Fe_3O_4@ZIF-8 after addition of 3 µM GSH at pH 7.5 and 10 µM GSH at pH 6.5. The left bar ('Top') represents the probe in the upper part of the Eppendorf, the right bar ('Bottom') the probe in the lower part of the Eppendorf.

As one can see in Figure 3.15, the Fe_3O_4@ZIF-8 displays significantly different heating efficiencies in different pH and GSH concentrations. In the sample representing healthy tissue, a SLP value of 54.3 W/g was encountered. In the sample representing the TME, this value increased by 27% to 69.3 W/g. Besides that, the lower probe resulted in lower SLP values, meaning that the samples were both well dispersed. The heating efficiency of the Fe_3O_4@ZIF-8 particles in the TME-like environment was still lower than the heating efficiency of the nanoparticles after synthesis (73.4 W/g, Figure 3.4), which indicates that still not all nanoparticles were fully released.

So while the difference between the two samples was larger than in case of the cysteine-based method and the final SLP value was slightly higher, this methodology is still not ideal. Assuming that all nanoparticles will be released, the hydrodynamic radius would be 67 nm, causing the diffusion coefficient to be $3.26 \cdot 10^{-12}$ m²/s. This diffusion coefficient would allow the particles to still be present within 500 µm from the injection site after one hour. Once again would the low diffusion coefficient cause the heating effect to be extremely local.

4

Conclusion

This thesis aimed to answer the research question *'How does the TME-biomarker GSH influence the magnetic hyperthermal properties of MNP for thermo-brachytherapy to treat early-stage breast cancer?'*. In the first stage of this thesis, nanoparticles were synthesised using co-precipitation. These particles had a mean physical diameter of 10±4 nm (Figure 3.3.E), which is slightly smaller than the ideal diameter of 13-15 nm. The heating efficiency was relatively high (SLP of 73.4 W/g) (Figure 3.4). After the addition of cysteine, the hydrodynamic radius increased from 67 nm to 209 nm (Figure 3.1). This, in combination with a decrease in heating efficiency (SLP of 61.4 W/g), could indicate aggregation to some extent. The addition of hydrogen peroxide increased the hydrodynamic radius to 323 nm and also decreased the heating efficiency even more (SLP of 59.1 W/g), which could indicate the nanoparticles aggregated even more. GSH had varying effects, depending on the concentration. A concentration of 3 µM GSH (extracellular concentration around healthy tissue) decreased the hydrodynamic radius (183 nm) and slightly increased the heating efficiency (SLP of 59.4 W/g). When adding 10 µM GSH (extracellular concentration in TME), the hydrodynamic radius decreased even more (172 nm) and the heating efficiency increased as well (66.0 W/g). However, when 10 mM GSH was added (intracellular GSH concentration in cancerous cells), the opposite effect was encountered. The hydrodynamic radius increased to 346 nm and the heating efficiency decreased to 30.7 W/g. This could indicate that 3 and 10 µM GSH promote dispersion, while 10 mM GSH promotes aggregation, which was also visualised with TEM (Figure 3.3.D). Another interesting result was that lower pH values had a negative effect on the dispersion of nanoparticles in samples with 10 µM GSH, but in samples with 10 mM GSH the pH value had no significant effect on either the dispersion or heating efficiency.

The diffusion of the cysteine-coated nanoparticles was also modelled and its influence on the temperature change at various distances from the injection site were analysed. Since the hydrodynamic radius was relatively large, the diffusion coefficient was low. This resulted in slow diffusion and therefore extremely localised heating (Figure 3.13, Figure 3.14).

For future research, it is strongly recommended to perform the FTIR once again with a larger amount of nanoparticles in order to obtain a stronger signal. It would also be interesting to analyse the reaction between cysteine itself (not bound to nanoparticles) after addition of hydrogen peroxide and GSH with Ellman's Test, NMR or MS for instance. This could be used as a proof of concept that the thiol/disulfide ratio is altered by the addition of hydrogen peroxide and GSH.

The heating efficiencies at 10 µM GSH were only 11% higher than at 3 µM GSH with the cysteine-based method. This indicates that if this methodology was used to achieve hyperthermia in TME, the healthy tissue would also be heated immensely. For this reason, an alternative methodology was also analysed. Uncoated nanoparticles were encapsulated in a ZIF-8 framework. The ZIF-8 based method resulted in a heating efficiency of 69.3 W/g in the TME-like environment, which is 27% higher than in healthy tissue-like environment (Figure 3.15). Due to time constrains, it was not possible to analyse the particles using TEM, FTIR or DLS. TEM could for instance provide valuable information regarding the size and geometry of the ZIF-8 structures. These frameworks could also be analysed on their

morphology before and after incubation at lower pH and higher GSH concentrations. TEM and DLS could provide insights in how the ZIF-8 framework might become less stable (framework shrinks or becomes more porous in tumour-like environments). Secondly, TEM and DLS could provide insights whether the difference in heating efficiencies is caused by the full release of nanoparticles or because the ZIF-8 structure has become less porous. This knowledge can help determine the mechanisms behind the ZIF-8 stability and the release kinetics of its nanoparticles. This could thereby guide the optimisation of the framework for the use of thermo-brachy therapy.

To conclude, this thesis was able to prove a slight increase (11%) in heating efficiency when comparing GSH concentrations related to cancerous tissue compared to healthy tissue with the cysteine-based approach. With the ZIF-8-based approach, this difference was 27%, which would cause less thermal damage to healthy tissue compared to the cysteine-based approach if these particles would be used for thermo-brachy therapy. However, one of the main challenges remaining for future research is to increase the diffusion coefficient of the nanoparticles.

References

[1] World Health Organization: WHO. “Global cancer burden growing, amidst mounting need for services”. In: (Feb. 2024). URL: https://www.who.int/news/item/01-02-2024-global-cancer-burden-growing--amidst-mounting-need-for-services.

[2] Nicole Anderson and M. Celeste Simon. “The tumor microenvironment”. In: *CB/Current biology* 30.16 (Aug. 2020), R921–R925. DOI: 10.1016/j.cub.2020.06.081. URL: https://doi.org/10.1016/j.cub.2020.06.081.

[3] Sungmun Lee and Aya Shanti. “Effect of exogenous pH on cell growth of breast cancer cells”. In: *International journal of molecular sciences* 22.18 (Sept. 2021), p. 9910. DOI: 10.3390/ijms22189910. URL: https://doi.org/10.3390/ijms22189910.

[4] Wei Wu et al. “Endogenous pH-responsive nanoparticles with programmable size changes for targeted tumor therapy and imaging applications”. In: *Theranostics* 8.11 (Jan. 2018), pp. 3038–3058. DOI: 10.7150/thno.23459. URL: https://doi.org/10.7150/thno.23459.

[5] Ankita Bansal and M. Celeste Simon. “Glutathione metabolism in cancer progression and treatment resistance”. In: *The journal of cell biology/The Journal of cell biology* 217.7 (June 2018), pp. 2291–2298. DOI: 10.1083/jcb.201804161. URL: https://doi.org/10.1083/jcb.201804161.

[6] Luke S. Kennedy et al. “Role of glutathione in cancer: From mechanisms to therapies”. In: *Biomolecules* 10.10 (Oct. 2020), p. 1429. DOI: 10.3390/biom10101429. URL: https://doi.org/10.3390/biom10101429.

[7] Iok In Christine Chio and David A. Tuveson. “ROS in Cancer: The burning question”. In: *Trends in molecular medicine* 23.5 (May 2017), pp. 411–429. DOI: 10.1016/j.molmed.2017.03.004. URL: https://doi.org/10.1016/j.molmed.2017.03.004.

[8] Chiara Gorrini, Isaac S. Harris, and Tak W. Mak. “Modulation of oxidative stress as an anticancer strategy”. In: *Nature reviews. Drug discover/Nature reviews. Drug discovery* 12.12 (Nov. 2013), pp. 931–947. DOI: 10.1038/nrd4002. URL: https://doi.org/10.1038/nrd4002.

[9] José M. Estrela, Ángel Ortega, and Elena Obrador. “Glutathione in cancer biology and therapy”. In: *Critical reviews in clinical laboratory sciences* 43.2 (Jan. 2006), pp. 143–181. DOI: 10.1080/10408360500523878. URL: https://doi.org/10.1080/10408360500523878.

[10] Chao-Yu Cui, Bin Li, and Xun-Cheng Su. “Real-Time monitoring of the level and activity of intracellular glutathione in live cells at atomic resolution by 19F-NMR”. In: *ACS central science* 9.8 (July 2023), pp. 1623–1632. DOI: 10.1021/acscentsci.3c00385. URL: https://doi.org/10.1021/acscentsci.3c00385.

[11] F Michelet et al. “Blood and plasma glutathione measured in healthy subjects by HPLC: relation to sex, aging, biological variables, and life habits”. In: *Clinical chemistry* 41.10 (Oct. 1995), pp. 1509–1517. DOI: 10.1093/clinchem/41.10.1509. URL: https://doi.org/10.1093/clinchem/41.10.1509.

[12] Wei Wang et al. “In vivo two photon visualization and quantitative detection of redox state of cancer”. In: *Journal of biophotonics* 15.5 (Jan. 2022). DOI: 10.1002/jbio.202100357. URL: https://doi.org/10.1002/jbio.202100357.

[13] Guoyao Wu et al. “Glutathione metabolism and its implications for health”. In: *The journal of nutrition/The Journal of nutrition* 134.3 (Mar. 2004), pp. 489–492. DOI: 10.1093/jn/134.3.489. URL: https://doi.org/10.1093/jn/134.3.489.

[14] *Treatment for cancer | Cancer Treatment Options*. URL: https://www.cancer.org/cancer/managing-cancer/treatment-types.html.

[15] Reanne Booker. “Palliative Radiation therapy: The role of radiation therapy in Palliative and End-of-Life care”. In: *Clinical Journal of Oncology Nursing* (Nov. 2022). DOI: 10.1188/22.cjon.628-635. URL: https://doi.org/10.1188/22.cjon.628-635.

[16] A Dietrich et al. “Improving external beam radiotherapy by combination with internal irradiation”. In: *The British journal of radiology/British journal of radiology* 88.1051 (July 2015), p. 20150042. DOI: 10.1259/bjr.20150042. URL: https://doi.org/10.1259/bjr.20150042.

[17] Janusz Skowronek. “Current status of brachytherapy in cancer treatment – short overview”. In: *Journal of Contemporary Brachytherapy* 9.6 (Jan. 2017), pp. 581–589. DOI: 10.5114/jcb.2017.72607. URL: https://doi.org/10.5114/jcb.2017.72607.

[18] Helena Gavilán et al. “Magnetic nanoparticles and clusters for magnetic hyperthermia: optimizing their heat performance and developing combinatorial therapies to tackle cancer”. In: *Chemical Society reviews* 50.20 (Jan. 2021), pp. 11614–11667. DOI: 10.1039/d1cs00427a. URL: https://doi.org/10.1039/d1cs00427a.

[19] Peter Vaupel and Michael R. Horsman. “Tumour perfusion and associated physiology: Characterization and significance for hyperthermia”. In: *International journal of hyperthermia* 26.3 (Jan. 2010), pp. 209–210. DOI: 10.3109/02656731003636436. URL: https://doi.org/10.3109/02656731003636436.

[20] Edward L. Gillette and Beverly A. Ensley. “Effect of heating order on radiation response of mouse tumor and skin”. In: *International journal of radiation oncology, biology, physics* 5.2 (Feb. 1979), pp. 209–213. DOI: 10.1016/0360-3016(79)90721-1. URL: https://doi.org/10.1016/0360-3016(79)90721-1.

[21] Jens Overgaard. “Simultaneous and sequential hyperthermia and radiation treatment of an experimental tumor and its surrounding normal tissue in vivo”. In: *International journal of radiation oncology, biology, physics* 6.11 (Nov. 1980), pp. 1507–1517. DOI: 10.1016/0360-3016(80)90008-5. URL: https://doi.org/10.1016/0360-3016(80)90008-5.

[22] Timothy M. Zagar et al. “Hyperthermia combined with radiation therapy for superficial breast cancer and chest wall recurrence: A review of the randomised data”. In: *International journal of hyperthermia* 26.7 (Sept. 2010), pp. 612–617. DOI: 10.3109/02656736.2010.487194. URL: https://doi.org/10.3109/02656736.2010.487194.

[23] Manuel A. González-Fernández et al. “Magnetic nanoparticles for power absorption: Optimizing size, shape and magnetic properties”. In: *Journal of solid state chemistry* 182.10 (Oct. 2009), pp. 2779–2784. DOI: 10.1016/j.jssc.2009.07.047. URL: https://doi.org/10.1016/j.jssc.2009.07.047.

[24] Alexandra Maier et al. “From Structure to Function: Understanding synthetic conditions in relation to magnetic properties of hybrid PD/FE-Oxide nanoparticles”. In: *Nanomaterials* 12.20 (Oct. 2022), p. 3649. DOI: 10.3390/nano12203649. URL: https://doi.org/10.3390/nano12203649.

[25] Daozhen Chen et al. “Biocompatibility of magnetic Fe3O4 nanoparticles and their cytotoxic effect on MCF-7 cells”. In: *International journal of nanomedicine* (Sept. 2012), p. 4973. DOI: 10.2147/ijn.s35140. URL: https://doi.org/10.2147/ijn.s35140.

[26] Sheng Tong et al. “Size-Dependent heating of magnetic iron oxide nanoparticles”. In: *ACS nano* 11.7 (June 2017), pp. 6808–6816. DOI: 10.1021/acsnano.7b01762. URL: https://doi.org/10.1021/acsnano.7b01762.

[27] Mark Klokkenburg, Jan Hilhorst, and Ben H. Erné. “Surface analysis of magnetite nanoparticles in cyclohexane solutions of oleic acid and oleylamine”. In: *Vibrational spectroscopy* 43.1 (Jan. 2007), pp. 243–248. DOI: 10.1016/j.vibspec.2006.09.008. URL: https://doi.org/10.1016/j.vibspec.2006.09.008.

[28] Dan Ma et al. “Redox-Sensitive clustered ultrasmall iron oxide nanoparticles for switchable T2/T1-Weighted magnetic resonance imaging applications”. In: *Bioconjugate chemistry* 31.2 (Nov. 2019), pp. 352–359. DOI: 10.1021/acs.bioconjchem.9b00659. URL: https://doi.org/10.1021/acs.bioconjchem.9b00659.

[29] Lin An et al. “pH and Glutathione Synergistically Triggered Release and Self-Assembly of Au Nanospheres for Tumor Theranostics”. In: *ACS applied materials & interfaces* 12.7 (Jan. 2020), pp. 8050–8061. DOI: 10.1021/acsami.0c00302. URL: https://doi.org/10.1021/acsami.0c00302.

[30] Grantley Creese. *What is Dynamic Light Scattering?* Apr. 2024. URL: https://www.brookhaveninstruments.com/what-is-dynamic-light-scattering/.

[31] Mathew Kallumadil et al. “Suitability of commercial colloids for magnetic hyperthermia”. In: *Journal of magnetism and magnetic materials* 321.10 (May 2009), pp. 1509–1513. DOI: 10.1016/j.jmmm.2009.02.075. URL: https://doi.org/10.1016/j.jmmm.2009.02.075.

[32] Luis C. Branquinho et al. “Effect of magnetic dipolar interactions on nanoparticle heating efficiency: Implications for cancer hyperthermia”. In: *Scientific reports* 3.1 (Oct. 2013). DOI: 10.1038/srep02887. URL: https://doi.org/10.1038/srep02887.

[33] P. De La Presa et al. “Study of heating efficiency as a function of concentration, size, and applied field in Γ-FE2O3 nanoparticles”. In: *Journal of physical chemistry. C./Journal of physical chemistry. C* 116.48 (Nov. 2012), pp. 25602–25610. DOI: 10.1021/jp310771p. URL: https://doi.org/10.1021/jp310771p.

[34] Wahajuddin and Sumit Arora. “Superparamagnetic iron oxide nanoparticles: magnetic nanoplatforms as drug carriers”. In: *International journal of nanomedicine* (July 2012), p. 3445. DOI: 10.2147/ijn.s30320. URL: https://doi.org/10.2147/ijn.s30320.

[35] Mini Namdeo et al. “Magnetic nanoparticles for drug delivery applications”. In: *Journal of nanoscience and nanotechnology* 8.7 (July 2008), pp. 3247–3271. DOI: 10.1166/jnn.2008.399. URL: https://doi.org/10.1166/jnn.2008.399.

[36] Yueh Hsia Luo, Louis W. Chang, and Pinpin Lin. “Metal-Based nanoparticles and the immune system: activation, inflammation, and potential applications”. In: *BioMed research international* 2015 (Jan. 2015), pp. 1–12. DOI: 10.1155/2015/143720. URL: https://doi.org/10.1155/2015/143720.

[37] Ahmad Fadli et al. “Synthesis of magnetite nanoparticles via co-precipitation method”. In: *IOP conference series. Materials science and engineering* 622.1 (Oct. 2019), p. 012013. DOI: 10.1088/1757-899x/622/1/012013. URL: https://doi.org/10.1088/1757-899x/622/1/012013.

[38] J. Sangeetha and John Philip. “Synthesis, characterization and antimicrobial property of Fe3O4-Cys-HNQ nanocomplex, with l-cysteine molecule as a linker”. In: *RSC advances* 3.21 (Jan. 2013), p. 8047. DOI: 10.1039/c3ra00005b. URL: https://doi.org/10.1039/c3ra00005b.

[39] Wenbo Wu et al. “Zeolitic Imidazolate Framework (ZIF-8) Decorated Iron Oxide Nanoparticles Loaded Doxorubicin Hydrochloride for Osteosarcoma Treatment - in vitro and in vivo Preclinical Studies”. In: *International journal of nanomedicine* Volume 18 (Dec. 2023), pp. 7985–7999. DOI: 10.2147/ijn.s438771. URL: https://doi.org/10.2147/ijn.s438771.

[40] *Electromagnetic fields and optical radiation in hospitals*. URL: https://www.rivm.nl/en/electromagnetic-fields/emf-optical-radiation-hospitals.

[41] UCSF Department of Radiology & Biomedical Imaging. *Potential hazards and risks*. Jan. 2018. URL: https://radiology.ucsf.edu/patient-care/patient-safety/mri/potential-hazards-risks#:~:text=Biological%20Effects%20Due%20to%20Magnetic,on%20cell%20growth%20and%20morphology..

[42] Dayong Luo, Scott W. Smith, and Bradley D. Anderson. “Kinetics and mechanism of the reaction of cysteine and hydrogen peroxide in aqueous solution”. In: *Journal of pharmaceutical sciences* 94.2 (Feb. 2005), pp. 304–316. DOI: 10.1002/jps.20253. URL: https://doi.org/10.1002/jps.20253.

[43] Carolyn S. Sevier and Chris A. Kaiser. “Formation and transfer of disulphide bonds in living cells”. In: *Nature reviews. Molecular cell biology* 3.11 (Nov. 2002), pp. 836–847. DOI: 10.1038/nrm954. URL: https://doi.org/10.1038/nrm954.

[44] Maria Tereza Cortez Fernandes et al. “The competing effect of ammonia in the synthesis of iron oxide/silica nanoparticles in microemulsion/sol–gel system”. In: *Colloids and surfaces. A, Physicochemical and engineering aspects* 422 (Apr. 2013), pp. 136–142. DOI: 10.1016/j.colsurfa.2013.01.025. URL: https://doi.org/10.1016/j.colsurfa.2013.01.025.

[45] Seyed Mohammadali Dadfar et al. “Size-isolation of superparamagnetic iron oxide nanoparticles improves MRI, MPI and hyperthermia performance”. In: *Journal of nanobiotechnology* 18.1 (Jan. 2020). DOI: 10.1186/s12951-020-0580-1. URL: https://doi.org/10.1186/s12951-020-0580-1.

[46] Benjamin Michen et al. “Avoiding drying-artifacts in transmission electron microscopy: Characterizing the size and colloidal state of nanoparticles”. In: *Scientific reports* 5.1 (May 2015). DOI: 10.1038/srep09793. URL: https://doi.org/10.1038/srep09793.

[47] C. Haase and U. Nowak. “Role of dipole-dipole interactions for hyperthermia heating of magnetic nanoparticle ensembles”. In: *Physical review. B, Condensed matter and materials physics* 85.4 (Jan. 2012). DOI: 10.1103/physrevb.85.045435. URL: https://doi.org/10.1103/physrevb.85.045435.

[48] Enzo Bertuit et al. “Angular orientation between the cores of iron oxide nanoclusters controls their magneto–optical properties and magnetic heating functions”. In: *Communications chemistry* 5.1 (Dec. 2022). DOI: 10.1038/s42004-022-00787-0. URL: https://doi.org/10.1038/s42004-022-00787-0.

[49] Asahi Tomitaka et al. “Heat dissipation and magnetic properties of surface-coated Fe3O4 nanoparticles for biomedical applications”. In: *Journal of magnetism and magnetic materials* 324.21 (Oct. 2012), pp. 3437–3442. DOI: 10.1016/j.jmmm.2012.02.060. URL: https://doi.org/10.1016/j.jmmm.2012.02.060.

[50] Satoshi Kokura, Toshikazu Yoshikawa, and Takeo Ohnishi. *Hyperthermic Oncology from Bench to Bedside*. Jan. 2016. DOI: 10.1007/978-981-10-0719-4. URL: https://doi.org/10.1007/978-981-10-0719-4.

[51] *GSH/GSSG-GLOTM Assay | Measure ratio of GSH to GSSG | ProMeGA*. URL: https://nld.promega.com/products/cell-health-assays/oxidative-stress-assays/gsh_gssg_glo-assay/?catNum=V6611.

[52] Reiko Matsui et al. “Redox RegulationviaGlutaredoxin-1 and ProteinS-Glutathionylation”. In: *Antioxidants and redox signaling* 32.10 (Apr. 2020), pp. 677–700. DOI: 10.1089/ars.2019.7963. URL: https://doi.org/10.1089/ars.2019.7963.

[53] Gohar Deilamy-Rad, Khadijeh Asghari, and Hossein Tavallali. “Development of a Reversible Indicator Displacement Assay Based on the 1-(2-Pyridylazo)-2-naphthol for Colorimetric Determination of Cysteine in Biological Samples and Its Application to Constructing the Paper Test Strips and a Molecular-Scale Set/Reset Memorized Device”. In: *Applied biochemistry and biotechnology* 192.1 (Apr. 2020), pp. 85–102. DOI: 10.1007/s12010-019-03165-0. URL: https://doi.org/10.1007/s12010-019-03165-0.

[54] Lana Burgess. *How does tumor size relate to breast cancer stage?* Dec. 2023. URL: https://www.medicalnewstoday.com/articles/325669#tumor-sizes.

[55] Yongsook C. Lee, Gary D. Fullerton, and Beth A. Goins. “Comparison of Multimodality Image-Based Volumes in Preclinical Tumor Models Using In-Air Micro-CT Image Volume as Reference Tumor Volume”. In: *Open journal of medical imaging* 05.03 (Jan. 2015), pp. 117–132. DOI: 10.4236/ojmi.2015.53016. URL: https://doi.org/10.4236/ojmi.2015.53016.

[56] Peter Vaupel and Helmut Piazena. “Strong correlation between specific heat capacity and water content in human tissues suggests preferred heat deposition in malignant tumors upon electromagnetic irradiation”. In: *International journal of hyperthermia* 39.1 (July 2022), pp. 987–997. DOI: 10.1080/02656736.2022.2067596. URL: https://doi.org/10.1080/02656736.2022.2067596.

[57] B.V. Harmon et al. “Cell Death Induced in a Murine Mastocytoma by 42–47°C Heatingin Vitro: Evidence that the Form of Death Changes from Apoptosis to Necrosis Above a Critical Heat Load”. In: *International journal of radiation biology* 58.5 (Jan. 1990), pp. 845–858. DOI: 10.1080/09553009014552221. URL: https://doi.org/10.1080/09553009014552221.

[58] Tianyu Du et al. “In situ multimodality imaging of cancerous cells based on a selective performance of FE2+-Adsorbed zeolitic imidazolate framework-8”. In: *Advanced functional materials* 27.5 (Dec. 2016). DOI: 10.1002/adfm.201603926. URL: https://doi.org/10.1002/adfm.201603926.

[59] Chun-Yi Sun et al. “Zeolitic imidazolate framework-8 as efficient pH-sensitive drug delivery vehicle”. In: *Dalton transactions* 41.23 (Jan. 2012), p. 6906. DOI: 10.1039/c2dt30357d. URL: https://doi.org/10.1039/c2dt30357d.

[60] Marcus Hoop et al. “Biocompatibility characteristics of the metal organic framework ZIF-8 for therapeutical applications”. In: *Applied materials today* 11 (June 2018), pp. 13–21. DOI: 10.1016/j.apmt.2017.12.014. URL: https://doi.org/10.1016/j.apmt.2017.12.014.

[61] Cátia Vieira Rocha et al. “PLGA-Based composites for various biomedical applications”. In: *International journal of molecular sciences* 23.4 (Feb. 2022), p. 2034. DOI: 10.3390/ijms23042034. URL: https://doi.org/10.3390/ijms23042034.

[62] Srinivasan Ayyanaar et al. “A novel curcumin-loaded PLGA micromagnetic composite system for controlled and pH-responsive drug delivery”. In: *Colloids and surfaces. A, Physicochemical and engineering aspects* 573 (July 2019), pp. 188–195. DOI: 10.1016/j.colsurfa.2019.04.062. URL: https://doi.org/10.1016/j.colsurfa.2019.04.062.

A

Appendix

A.1. Data Dynamic Light Scattering

Figure A.1 shows all obtained normalised correlation functions. The hydrodynamic radii from Section 3.2 and Section 3.7 were derived from these functions.

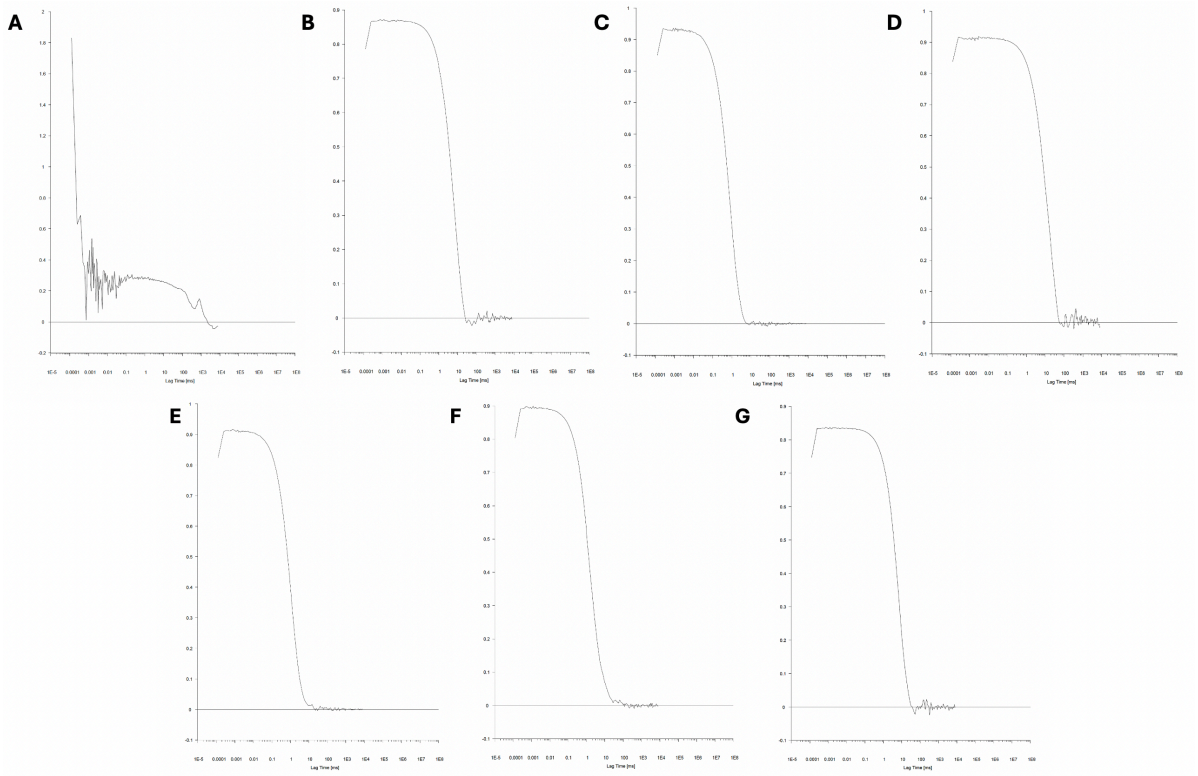

Figure A.1: All obtained normalised correlation functions during DLS. **A)** MilliQ. **B)** After synthesis. **C)** After Cys addition. **D)** After H_2O_2 addition. **E)** After 3 µM GSH addition. **F)** After 10 µM GSH addition. **G)** After 10 mM GSH addition.

A.2. Data heating experiments

Table A.1 to Table A.5 show the data used to calculate each SLP value. The sample, the mass (determined with ICP-MS), temperature change (per probe) and SLP value (per probe) are given. Table A.1 shows the data used for Figure 3.4 in Section 3.5, Table A.2 shows the data used for Figure 3.9 in Section 3.6, Table A.3 shows the data used for Figure 3.10 in Section 3.7.1, Table A.4 shows the data used for Figure 3.12 in Section 3.7.2 and Table A.5 shows the data used for Figure 3.15 in Section

3.9.1. To calculate all SLP values, Equation 2.1 was used, assuming a specific heat capacity of 4186 J/(kg K) and a heating time (Δt) of 290 seconds.

Table A.1: Sample Data with Probe Locations, Temperature Changes, and SLP Values used for Figure 3.4 in Section 3.5.

Sample	Mass (mg)	Probe Location	Temperature Change (°C)	SLP (W/g)
After synthesis	3.6	Upper Lower	18.39 14.72	73.4 58.7
After Cys	3.4	Upper Lower	14.25 10.33	61.4 44.5
After H_2O_2	2.2	Upper Lower	8.90 6.93	59.1 46.0
After 10 µM GSH	2.2	Upper Lower	9.93 7.76	66.0 51.6

Table A.2: Sample Data with Probe Locations, Temperature Changes, and SLP Values used for Figure 3.9 in Section 3.6.

Sample	Mass (mg)	Probe Location	Temperature Change (°C)	SLP (W/g)
After H_2O_2	2.2	Upper Lower	8.90 6.93	59.1 46.0
After 3 µM GSH	2.2	Upper Lower	8.94 6.77	59.4 45.0
After 10 µM GSH	2.2	Upper Lower	9.93 7.76	66.0 51.6
After 10 mM GSH	2.8	Upper Lower	5.82 7.76	30.7 35.5

Table A.3: Sample Data with Probe Locations, Temperature Changes, and SLP Values used for Figure 3.10 in Section 3.7.1.

Sample	Mass (mg)	Probe Location	Temperature Change (°C)	SLP (W/g)
10 µM GSH, pH = 5.5	2.2	Upper Lower	9.93 7.76	66.0 51.6
10 µM GSH, pH = 6.5	2.2	Upper Lower	9.79 7.86	65.0 52.2
10 µM GSH, pH = 7.5	2.2	Upper Lower	9.64 7.90	64.0 52.5
10 µM GSH, pH = 8.5	2.2	Upper Lower	10.55 8.44	70.1 56.1

Table A.4: Sample Data with Probe Locations, Temperature Changes, and SLP Values used for Figure 3.12 in Section 3.7.2.

Sample	Mass (mg)	Probe Location	Temperature Change (°C)	SLP (W/g)
10 mM GSH, pH = 4.5	2.8	Upper Lower	5.82 6.75	30.7 35.5
10 mM GSH, pH = 6.5	2.8	Upper Lower	8.91 16.69	46.9 87.9
10 mM GSH, pH = 8.5	2.8	Upper Lower	14.39 19.41	50.0 102.2

Table A.5: Sample Data with Probe Locations, Temperature Changes, and SLP Values used for Figure 3.15 in Section 3.9.1.

Sample	Mass (mg)	Probe Location	Temperature Change (°C)	SLP (W/g)
3 µM GSH, pH = 7.5	3.6	Upper	13.62	54.3
		Lower	9.86	39.3
10 µM GSH, pH = 6.5	1.8	Upper	8.68	69.3
		Lower	6.36	50.7

A.3. Source code for the concentration and mass distribution over time

The following code presents the model used in Figure 3.13 in Section 3.8.1.

```
import numpy as np
import matplotlib.pyplot as plt

L = 0.01  # Length of the tumor (m)
Nx = 100  # Number of spatial points
dx = L / (Nx - 1)  # Spatial step size (m)
T = 3600  # Total simulation time (s)
Nt = 500  # Number of time steps
dt = T / Nt  # Time step size (s)
C = np.zeros((Nt, Nx))
initial_concentration_mg_per_mL = 10.0 # Initial concentration in mg/mL
C[0, Nx // 2] = initial_concentration_mg_per_mL / 1e9 # Assume it is injected in the middle
    of the tumour (kg/m³)

for n in range(Nt - 1): # Diffusion simulation using explicit finite difference method
    for i in range(1, Nx - 1):
        C[n + 1, i] = C[n, i] + D_water * dt * (C[n, i + 1] - 2 * C[n, i] + C[n, i - 1]) /
            dx**2

C_mg_per_mL = C * 1e9 # concentration to mg/mL assuming a density of 1.079 g/cm³
x_cm = np.linspace(0, L, Nx) * 100 # Convert x to centimeters

plt.figure(figsize=(10, 6))
plt.plot(x_cm, C_mg_per_mL[0, :], label='Concentration directly after injection')
plt.plot(x_cm, C_mg_per_mL[Nt // 2, :], label=f'Concentration after {T / 2 / 60} minutes')
plt.plot(x_cm, C_mg_per_mL[-1, :], label=f'Concentration after {T / 60} minutes')
plt.xlabel('Location in tumour (cm)')
plt.ylabel('Nanoparticle concentration (mg/mL)')
plt.legend()
plt.grid(True)
plt.show()
```

```
D_water = 1.268e-12  # Diffusion coefficient of nanoparticles calculated based of the
    hydrodynamic radius after addition of 10 µM GSH based of DLS
radius_m = 10.1 * 1.0e-9  # Radius of nanoparticles in nanometers based of TEM
mass_mg = 0.9  # Initial mass of nanoparticles in mg

L = 0.01  # Length of the tumor (m)
Nx = 100  # Number of spatial points
dx = L / (Nx - 1)  # Spatial step size (m)
T = 3600  # Total simulation time (s)
Nt = 500  # Number of time steps
dt = T / Nt  # Time step size (s)

C = np.zeros((Nt, Nx))

volume_element_m3 = dx**3  # Volume of each spatial element in m³
# Initial condition: Mass of nanoparticles at the center
initial_concentration_kg_per_m3 = mass_mg / 1e6 / volume_element_m3  # Convert mg to kg and
    divide by volume element (dx³)
C[0, Nx // 2] = initial_concentration_kg_per_m3

for n in range(Nt - 1): # Diffusion simulation using explicit finite difference method
    for i in range(1, Nx - 1):
```

```
        C[n + 1, i] = C[n, i] + D_water * dt * (C[n, i + 1] - 2 * C[n, i] + C[n, i - 1]) /
            dx**2

mass_mg_grid = C * volume_element_m3 * 1e6  # Convert mass to mg

x_cm = np.linspace(0, L, Nx)*100  # Convert x to centimeters

plt.figure(figsize=(10, 6))
plt.plot(x_cm, mass_mg_grid[0, :], label='Mass directly after injection')
plt.plot(x_cm, mass_mg_grid[Nt // 2, :], label=f'Mass after {T / 2 / 60:.1f} minutes')
plt.plot(x_cm, mass_mg_grid[-1, :], label=f'Mass after {T / 60:.1f} minutes')
plt.xlabel('Location in tumour (cm)')
plt.ylabel('Nanoparticle mass (mg)')
plt.legend()
plt.grid(True)
plt.show()
```

A.4. Source code for the heat distribution over time

The following code presents the model used in Figure 3.14 in Section 3.8.1.

```
L = 0.01  # Length of the tumor (m)
Nx = 100  # Number of spatial points
dx = L / (Nx - 1)  # Spatial step size
T = 3600  # Total simulation time (s)
Nt = 500  # Number of time steps
dt = T / Nt  # Time step size

SLP = 66.0  # Specific Loss Power (SLP) in W/g
mass_tumor_g = 0.56  # Mass of the tumor in grams
specific_heat_J_gK = 3.75  # Specific heat capacity of the tumor in J/kg·K
time_s = np.linspace(0, T, Nt)  # Time range from 0 to T seconds

idx_injection_site = Nx // 2 #Injected in the middle of the tumour
mass_np_g_injection_site = mass_mg_grid[:, idx_injection_site] * 1e-3  # Convert mg to g
mass_np_g_injection_site_plus100 = mass_mg_grid[:, 51] * 1e-3  # Convert mg to g
mass_np_g_injection_site_plus200 = mass_mg_grid[:, 52] * 1e-3  # Convert mg to g
mass_np_g_injection_site_plus300 = mass_mg_grid[:, 53] * 1e-3  # Convert mg to g

deltaT_injection_site = (SLP * time_s * mass_np_g_injection_site) / (mass_tumor_g *
    specific_heat_J_gK)
deltaT_injection_site_plus100 = (SLP * time_s * mass_np_g_injection_site_plus100) /
    (mass_tumor_g * specific_heat_J_gK)
deltaT_injection_site_plus200 = (SLP * time_s * mass_np_g_injection_site_plus200) /
    (mass_tumor_g * specific_heat_J_gK)
deltaT_injection_site_plus300 = (SLP * time_s * mass_np_g_injection_site_plus300) /
    (mass_tumor_g * specific_heat_J_gK)

time_minutes = time_s / 60

plt.figure(figsize=(10, 6))
plt.plot(time_minutes, deltaT_injection_site, label='At the injection site')
plt.plot(time_minutes, deltaT_injection_site_plus100, label='100 µm from injection site')
plt.plot(time_minutes, deltaT_injection_site_plus200, label='200 µm from injection site')
plt.plot(time_minutes, deltaT_injection_site_plus300, label='300 µm from injection site')
plt.xlabel('Time (minutes)')
plt.ylabel('Temperature Change (°C)')
plt.legend()
plt.grid(True)
plt.show()
```